

UNIVERSITY OF LEOBEN
DEPARTMENT OF MATERIALS PHYSICS

Microstructural Evolution of Cu-Fe-Co and Ag-Fe-Co Composites Processed by High-Pressure Torsion

Bachelor Thesis



Spuller Mirjam
Leoben, June 2018

Affidavit

I declare in lieu of oath, that I wrote this thesis and performed the associated research myself, using only literature cited in this volume.

Leoben, June 2018

Place, Date

Spuller Mirjam

Abstract

In this bachelor thesis, the microstructural evolution of high-pressure torsion deformed samples of the ternary Cu-Fe-Co and Ag-Fe-Co system, which have different compositions, were investigated. The initial samples were produced by a powder metallurgy process and afterwards deformed by high-pressure torsion to create composites with nanostructured ferro- and diamagnetic phases similar to mechanically alloyed granular composites consisting of the same phases. To study the influence of the initial composite structure on the microstructural evolution during high-pressure torsion deformation, previous annealing treatments on chosen compositions were carried out as well.

It was observed that the deformation of the different samples of both ternary systems did not lead to the desired microstructure. Even at the position where the applied strain is the highest, the Co and Fe phases did not achieve the theoretical size of a few tens of nanometers. More or less large Co or Fe particles were still found in the final microstructure. Furthermore, the previous annealing treatments had hardly any influence of the deformation behaviour. However, in all samples a nanostructured microstructure of the Cu- or Ag-matrix with a possible partial supersaturation could be generated during the high-pressure torsion deformation process.

Contents

1. Introduction	1
2. Theory.....	2
2.1. Mechanically alloyed Cu-Fe-Co and Ag-Fe-Co	2
2.2. High-pressure torsion (HPT)	4
2.2.1. Differences in deformation of single phase and composite materials	6
3. Materials and Experiments	8
4. Results.....	11
4.1. Structural evolution as function of applied strain	11
4.2. Influence of an initial annealing treatment on structural evolution	14
4.3. Phase Analysis with ImageJ.....	19
Chemical phase analyses with EDX.....	24
4.4. Microhardness as function of applied strain	29
5. Discussion	31
6. Conclusion and Outlook.....	33
8. List of Figures	36
9. List of Tables	38
10. List of references	39
11. Appendix	41
11.1. Evolution of the microstructure.....	41
11.2. Results of the phase analysis with ImageJ	44

1. Introduction

Due to the technically attractive magnetic and magnetoresistive properties of granular alloys, a lot of research and development have been taken place in this field for the last decades [1]. Granular alloys are composite materials similar to multilayers of alternating ferromagnetic and non-magnetic layers, which consist of nanometre-scaled diamagnetic and ferromagnetic phases. Examples are materials with fine-dispersed Fe-Co nanoparticles that are embedded in a conductive matrix of Cu or Ag [2]. Due to that particular microstructure, they also exhibit the giant magnetoresistance (GMR) effect, which is an enormous change in electric resistance when a magnetic field is applied; this effect can, for example, be used technologically in the data storage industry. One typical application is in a read head for magnetic recording [3]. To produce these granular alloys several methods, like sputtering, co-evaporation, ion implantation, melt spinning, sol-gel synthesis, and mechanical alloying (MA), can be used [4].

Another method, which enables the formation of ultra-fine grained or nanocrystalline bulk materials, is high-pressure torsion (HPT), a severe plastic deformation (SPD) technique. With this method – similar to mechanical alloying – supersaturated solid solutions of immiscible elements can be produced in a simple and cost-effective way. Due to the high degree of deformation during the HPT process, grain refinement takes place; therefore nanostructured composite materials with application-specific properties can be generated as well [5].

The aim of this thesis was to produce nanostructured bulk materials by HPT, which have a comparable microstructure and thus, the same magnetic properties as the granular alloys produced by the above-mentioned techniques. Therefore, various compositions of two ternary systems, Cu-Fe-Co and Ag-Fe-Co, already investigated intensively by MA [4,7], were selected. Powder-metallurgically produced samples were deformed by HPT, and the microstructural evolution was analysed by different methods. In addition, the influence of the initial composite structure on the microstructural development during the HPT deformation was studied.

2. Theory

2.1. Mechanically alloyed Cu-Fe-Co and Ag-Fe-Co

A production method of granular alloys is MA; this method is a solid state powder processing technique. Mixtures of powders (different pure metals, alloys, or compounds) are milled together in a high-energy ball mill. Due to repetitive welding, fracturing, and rewelding of the powder particles, MA is a capable procedure to generate a variety of equilibrium and non-equilibrium alloy phases. The last-named also involves supersaturated solid solutions of usually immiscible elements. Furthermore, with MA it is possible to create nanostructured bulk materials at low temperatures [6]. MA, as well as the HPT deformation process is a SPD technique, but after milling a further compaction step is needed to obtain bulk samples. Furthermore, contamination of the powders during the process due to abrasion of the milling balls can take place. Compared to HPT deformation, the amount of applied strain and the process parameters, for example the strain rate, cannot be precisely controlled during MA.

With MA it is further possible to produce granular alloys which show the GMR effect. To achieve this, various compositions of the ternary Cu-Fe-Co and Ag-Fe-Co systems are used [4,7]. In each case, Cu or Ag forms the conductive matrix, where particles of magnetic Fe, Co, or Fe-Co are embedded. Under equilibrium conditions, Co is miscible with Fe, and thus can form Fe-Co alloys with various compositions, whereas, the mutual solubility of Fe and Co in Cu and Ag can be considered as zero (Figure 1 and 2) [7].

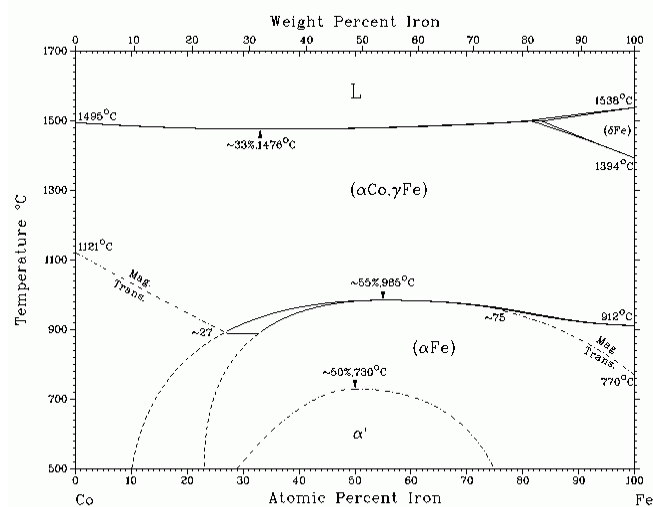


Figure 1: The Co-Fe phase diagram shows the miscibility of Fe and Co under equilibrium conditions [8].

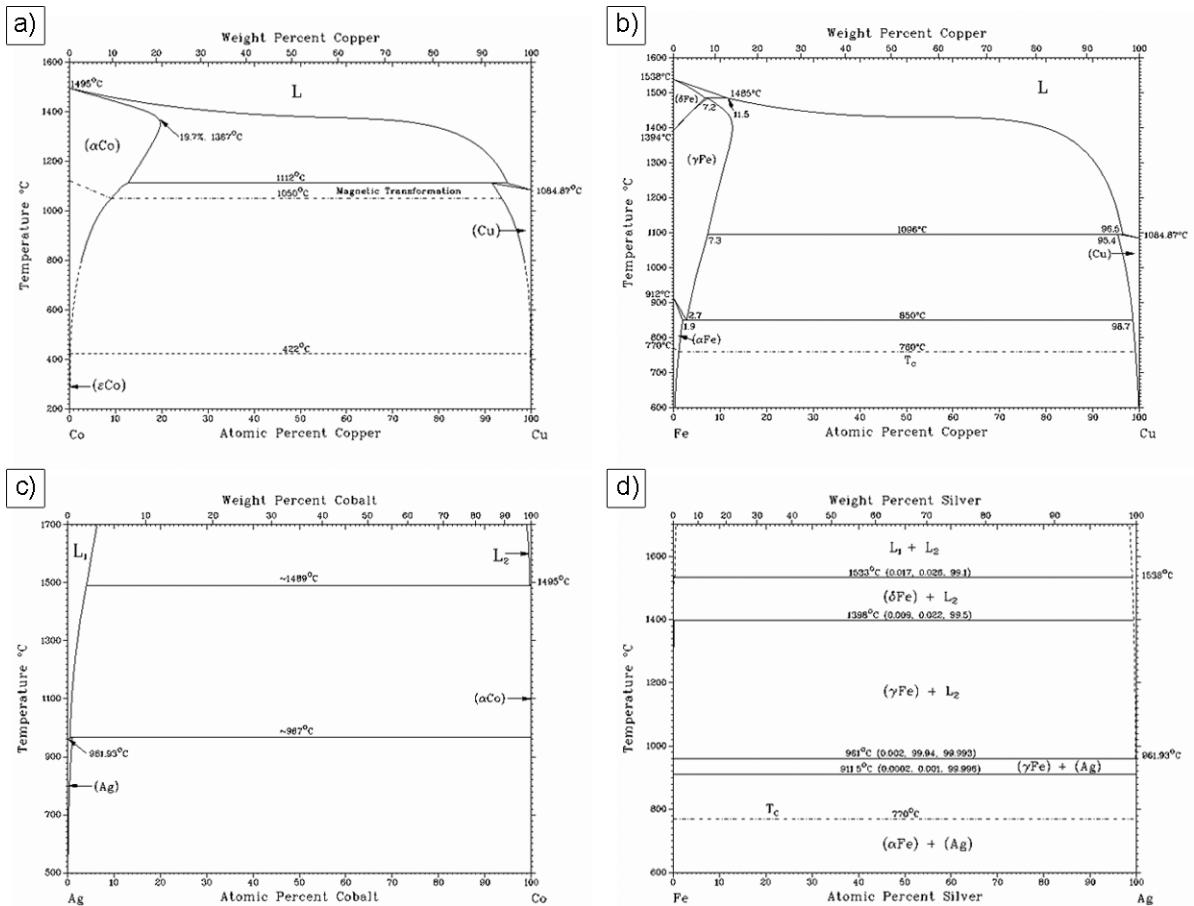


Figure 2: Phase diagrams of the binary immiscible systems: a) Co-Cu [9], b) Fe-Cu [10], c) Ag-Co [11] and Fe-Ag [12].

Previous investigations of the ternary Cu-Fe-Co system have shown that there are two possible procedures to form a specific microstructure, which leads to high values of magnetoresistance. The first one is that a stoichiometric mixture of the three elemental powders is milled by MA. During milling, Fe- and Co- atoms are dissolved in the Cu-matrix; the result of the milling process is a solid solution with an inhomogeneous distribution of Fe and Co atoms in the matrix material. A subsequent annealing treatment causes phase separation, and Fe-Co alloy phases are precipitated; these phases are finely distributed throughout the microstructure and responsible for the magnetic and magnetoresistive properties. The second production method is that pure Fe and Co powders are milled in a first step to create Fe-Co alloy powders. These powders are milled with Cu in a second milling process. The procedure leads to a microstructure which is comparable to the one processed by the first method. However, the first procedure is preferable to obtain materials with optimized magnetoresistive properties [2].

N.S. Cohen et. al. [4] further showed that after milling Ag powder with Fe-Co alloy powders, a dispersion of fine Fe-Co particles in a Ag matrix can be obtained after

milling. Additionally, a limited degree of alloying between Fe and Ag grains is observed; especially in samples that contain Fe-Co particles, which have high contents of Co, for example in the investigated $\text{Ag}_y(\text{Fe}_{0.15}\text{Co}_{0.85})_{1-y}$ samples. In this study, it was further shown that the $\text{Ag}_{70}(\text{Fe}_x\text{Co}_{1-x})_{30}$ samples have a consistently higher magnetoresistance than the $\text{Ag}_{50}(\text{Fe}_x\text{Co}_{1-x})_{50}$ samples. Since the $\text{Ag}_{70}(\text{Fe}_{0.15}\text{Co}_{0.85})_{30}$ samples show the largest magnetoresistance, it was determined that the amount and the composition of Fe-Co grains, as well as the alloying behaviour of the magnetic and non-magnetic phases, play a role in the production of granular alloys [4].

2.2. High-pressure torsion (HPT)

HPT is one type of SPD technique, which has been improved and further developed in the last 25 years [13]. The technique aroused great interest among material scientists due to the enormous amount of grain refinement, which can be achieved during the deformation process. Thus, in single phase materials ultrafine grains and even grain sizes in the nanometer range can be obtained. Due to the ultrafine or nanostructured microstructure, HPT deformed materials have considerably improved physical and mechanical properties like high values in ductility and strength [14]. Besides, powder consolidation and the production of supersaturated solid solutions are possible applications for HPT [16].

For the HPT deformation process a disc shaped sample is placed between two anvils. Both anvils have cylindrical, slightly conical cavities, whereby their total volume is a little bit smaller than the volume of the sample. After applying a pressure of 1-10 GPa, the two anvils are rotated with respect to each other. Depending on the material, a specific minimum pressure is necessary to prevent sliding between sample and the anvils. Additionally, the sample and the cavities of the anvils are sandblasted to create a microroughness and provide sufficient friction; therefore a constant torsion deformation is executable. Due to the smaller volume of the anvils cavities, a small amount of material flows out of the cavities. This material flow avoids a touching of the anvils and thus, an abrasion during the rotational movement. Furthermore, the material flow causes a hydrostatic pressure within the processing zone, because it becomes confined between the anvils, and this leads to a certain back pressure. A schematic illustration of the HPT equipment is shown in Figure 3a. Figure 3b shows the disc shaped sample and the definition of the different observation directions that are commonly used (axial, radial, and tangential) in the SPD community. The HPT deformation can be executed at temperatures between -196 and 500°C; therefore the anvils are cooled or heated to the desired temperature. Other process parameters, which can be varied, are the

rotational speed and the rotational direction of the anvils. Furthermore, with strain gauges, the torque, which is applied to the sample, can be determined in-situ during the deformation process. The controllability of the mentioned process parameters is a big advantage of HPT compared to other SPD techniques and the MA process [5,14].

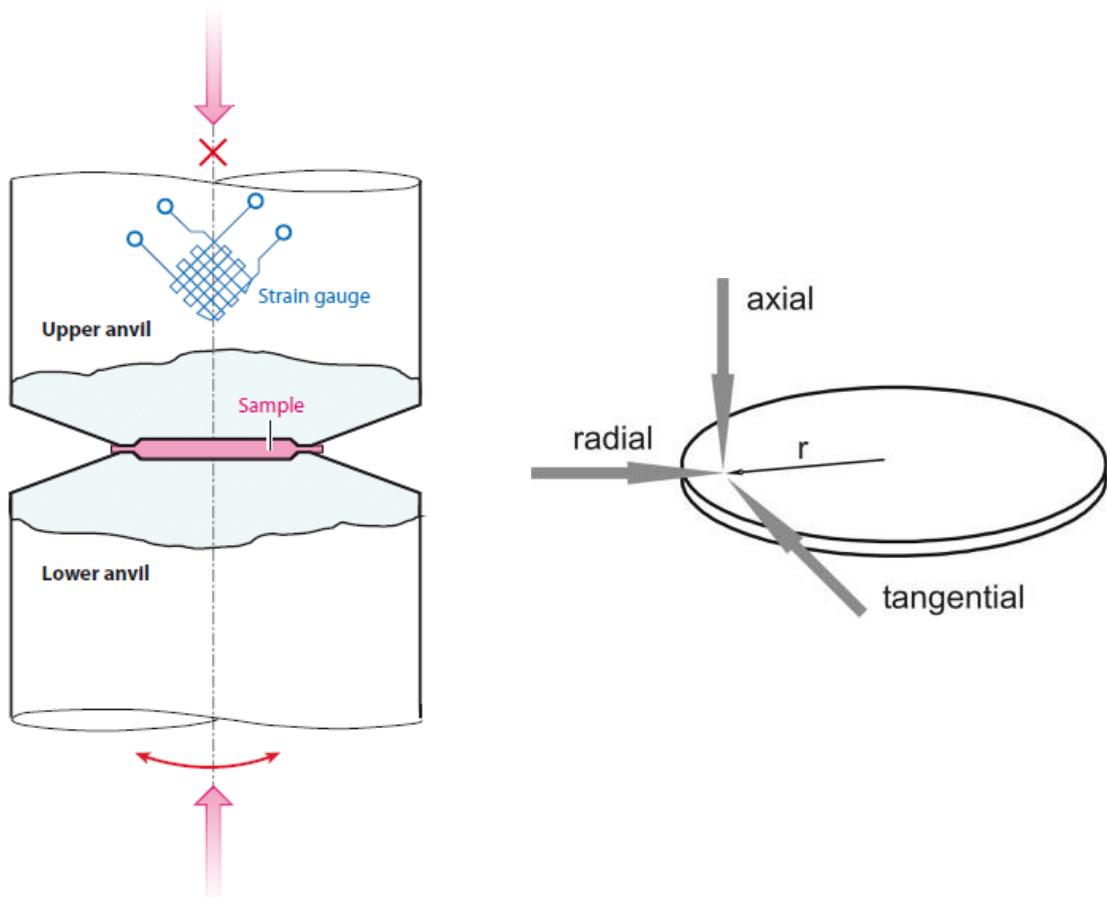


Figure 3: Schematic representation of a) the HPT equipment [13] and b) the disk shaped sample showing the different observation directions (axial, radial and tangential) [14].

A great advantage of the HPT deformation process is the simple procedure to obtain extremely high strains at relatively low temperatures. Therefore, it is an excellent method to investigate the behaviour of a material at this high degree of plastic deformation. The HPT deformation process is a simple shear one, and the shear strain γ can be calculated according to

$$\gamma = \frac{2\pi r}{t} n \quad (1)$$

where r , n , and t are the distance from the centre of the rotation axis, the number of revolutions, and the thickness of the sample, respectively.

The von Mises equivalent strain ε_{vm} is then [15]

$$\varepsilon_{VM} = \frac{\gamma}{\sqrt{3}} = \frac{2\pi r}{t\sqrt{3}} n. \quad (2)$$

Since it is easily possible to deform a sample with a thickness of 0.8 mm, for example, for 10 or 100 revolutions, the achieved equivalent strain at a radius of 4 mm is 200 or 2000, respectively. No other SPD technique enables to apply such high values of strains [14].

The greatest disadvantage of the HPT deformation process is the restricted sample size. As a consequence, this technique might be unattractive for many applications where a large sample size is required. However, there has been a permanent enhancement to upscale the size the HPT processed materials samples in the last few years [16].

2.2.1. Differences in deformation of single phase and composite materials

Independent of the initial microstructure or rather the initial grain size of pure metals and single phase materials, there is a specific minimum grain size, which can be achieved during HPT deformation. It does not matter if the initial grain size is coarser or finer; the refinement process saturates at a certain material specific strain [13]. But what happens during the deformation, and what leads to the grain refinement? When a single phase material is deformed, a production and a new arrangement of dislocations take place. As a result, new grain boundaries are formed, which split the initial grains. Thus, a microstructure with ultrafine or even nanocrystalline grains is achieved during the deformation process. However, after a certain amount of applied strain, an equilibrium between grain refinement and recovery processes occurs, and a steady state or saturation regime is reached. In this saturation regime, the grain size and consequently the hardness of the deformed material is invariable, also if higher strains are applied. Alloying elements, impurities and the deformation temperature are effective means to change the saturation grain size [5]. The minimum grain size, which can be obtained in composite materials, is significantly smaller compared to HPT deformed pure metals [14]. Furthermore, higher strains are needed to reach saturation in composite material, mostly due to complex fragmentation processes during deformation. In this case, it is also possible that no steady state is achievable with a reasonable amount of strain. In composite materials, the volume elements or different phases (characterised by, for example, their volume fraction, their arrangement, and their individual mechanical properties) are decisive for the evolution of the microstructure [5]. To produce a nanostructured composite by HPT,

the change of the shape of different phases during the deformation process is very important. The final size of the components after the deformation process d_{HPT} can be calculated with

$$d_{HPT} = \frac{d_0}{\gamma} \quad (3)$$

where d_0 is the initial size of the phases and γ the applied shear strain. Equation (3) is only valid if the composite material is ideally co-deformed during HPT deformation [17].

Furthermore, a supersaturated solid solution can be formed from a starting material, which consists of two or more immiscible elements during severe deformation by HPT. This enables the production of composites, which have an ultrafine grained, or nanocrystalline microstructure with partial or full supersaturation and consequently in modern days useful properties. For example, nanostructured Cu-Fe alloys show large magnetoresistive effects, and Cu-Co composites also display a GMR effect [5].

3. Materials and Experiments

For this thesis, two different ternary systems were investigated, namely the Cu-Fe-Co and Ag-Fe-Co system. The elemental metal powders of Cu, Ag, Co, and Fe (all 99.9% purity) were mixed in an autoclave in an inert argon atmosphere to obtain different compositions. Table 1 shows an overview of the investigated compositions in atomic percent (at%).

$\text{Cu}_y(\text{Fe}_{1-x}\text{Co}_x)_{100-y}$	$\text{Ag}_y(\text{Fe}_{1-x}\text{Co}_x)_{100-y}$
$\text{Cu}_{80}(\text{Fe}_{0.7}\text{Co}_{0.3})_{20}$	$\text{Ag}_{70}(\text{Fe}_{0.15}\text{Co}_{0.85})_{30}$
$\text{Cu}_{80}(\text{Fe}_{0.5}\text{Co}_{0.5})_{20}$	$\text{Ag}_{70}(\text{Fe}_{0.3}\text{Co}_{0.7})_{30}$
$\text{Cu}_{80}(\text{Fe}_{0.3}\text{Co}_{0.7})_{20}$	$\text{Ag}_{70}(\text{Fe}_{0.5}\text{Co}_{0.5})_{30}$
	$\text{Ag}_{50}(\text{Fe}_{0.15}\text{Co}_{0.85})_{50}$

Table 1: Overview of the investigated compositions (in at%) of the mixed powders.

The HPT tool was used to consolidate the powder blends; the mixed powders were filled in the grooved steel anvils and were compacted with an applied pressure of 5 GPa, a rotational speed of 0.2 rpm for 20 seconds. Afterwards, the precompact samples were HPT deformed with a different set of anvils, which have a shallower depth of the groove compared to the anvils that are used for the powder consolidation. The deformation parameters for all samples were the following: 5 GPa applied pressure, a rotational speed of 0.6 rpm, and 50 rotations. The consolidation and the deformation process were carried out at room temperature. To prevent heating of the sample during the deformation, the anvils and the sample were cooled with compressed air.

After the HPT processing, the samples were approximately 8 mm in diameter with a thickness of 0.4 mm. The resulting shear strain γ of the deformed samples can be calculated with Equation (1) and are shown in Table 2. Due to the slightly different dimensions of the samples, the given values of the shear strain are approximate ones.

r [mm]	0	1	2	3
$\gamma [-]$	0	785	1570	2356

Table 2: Values of the resulting shear strain γ at different positions in radial direction.

Microstructure analyses were carried out with a Zeiss Leo 1525 scanning electron microscope (SEM) and a light optical microscope (LOM). The deformed samples were cut in the middle, embedded in conductive resin and fine polished so that the

cut surface could be investigated. With the SEM, micrographs were taken with the back-scattered-electron (BSE) detector at the centre of the sample (0 mm) and at a radius of approximately 1, 2 and 3 mm. At every radii, BSE micrographs were taken with different magnifications (600x, 5000x, 24800x, and 50000x) to analyse the evolution of the microstructure and the deformation behaviour. To perform a phase analysis with ImageJ, which is an image processing software, micrographs were taken with the LOM at the same positions as with the SEM. For a more precise analysis, light optical micrographs were taken with a higher magnification (50x). For this reason, it was necessary to take more images at one radii and merge them. Therefore, Adobe Photoshop was used.

To study the influence of an initial annealing treatment on the deformation behaviour, one composition of $\text{Cu}_y(\text{Fe}_{1-x}\text{Co}_x)_{100-y}$ and one of $\text{Ag}_y(\text{Fe}_{1-x}\text{Co}_x)_{100-y}$ were chosen, namely $\text{Cu}_{80}(\text{Fe}_{0.5}\text{Co}_{0.5})_{20}$ and $\text{Ag}_{70}(\text{Fe}_{0.15}\text{Co}_{0.85})_{30}$. The precompacted samples were isothermally annealed at 500°C for 60 minutes and at 600°C for 30 minutes. HPT deformation of the samples was performed afterwards. For the deformation process, the same parameters as for the un-annealed and only compacted samples were applied. For further investigations of the microstructural evolution during annealing, a longer annealing time (120 minutes at 500°C and 600°C) was chosen as well.

Vickers Hardness of all HPT deformed samples was measured along the radii using a Buehler Micromet 5100. Every 0.5 mm a measurement with a load of 300 g (HV0.3) was carried out. To determine the influence of annealing on the hardness of the matrix material and the various particles, individual measurements in the different components (matrix and particles) with a load of 50 g (HV0.05) were performed.

Analyses of the existing phases in the deformed samples were executed with ImageJ. In these analyses the number of the particles and the feret diameter of the particles, viz. the distance between two parallel planes, which enclose a particle along a specific direction [18], were determined. For this investigation, the merged LOM micrographs were used. From these micrographs a picture section of 350 x 350 μm^2 were taken. Subsequently, the micrographs were converted in 8-bit images, and an individually defined threshold-level selects the particles from the matrix. The software displays the calculated result in a table and an image with the contours of the individual particles. The results of the analyses were evaluated by Microsoft Excel where the feret diameter of the particles was categorized, and the frequency was determined.

Energy-dispersive X-ray (EDX) analyses were carried out with the Zeiss Leo 1525 SEM, in order to characterise the chemical composition of the occurring phases. For each EDX measurement, the same parameters (for example aperture size, acceleration voltage and counts) were used.

4. Results

4.1. Structural evolution as function of applied strain

In Figure 4, the evolution of the microstructure of the deformed $\text{Cu}_{80}(\text{Fe}_{0.5}\text{Co}_{0.5})_{20}$ sample is shown. The BSE micrographs were taken at radius 0, 1, 2, and 3 mm. Since the observed microstructural evolution during HPT deformation of all three different Cu-Fe-Co compositions were very similar, these micrographs represent the behaviour of all investigated samples of this ternary system. The micrographs of the other Cu-Fe-Co samples can be found in the appendix.

After the HPT deformation, there are remaining particles of Co and Fe along the whole radius visible (Figure 4). With increasing strain, however, many particles are dissolved in the matrix or become smaller than the resolution at the used magnification. Nonetheless, there are also some large particles at a radius of 3 mm visible, where the applied strain is very high.

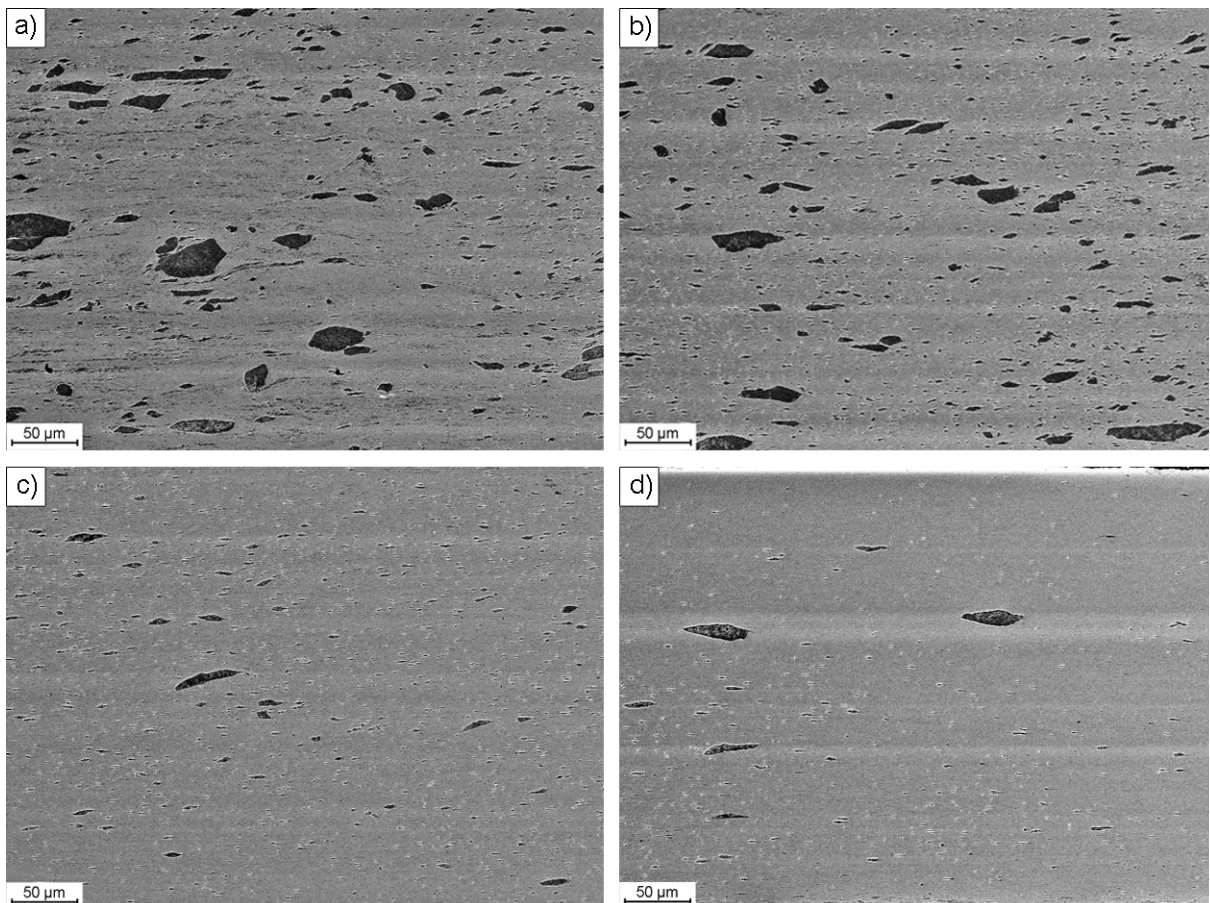


Figure 4: BSE micrographs of the microstructure of the deformed $\text{Cu}_{80}(\text{Fe}_{0.5}\text{Co}_{0.5})_{20}$ sample at a radius of a) 0 mm b) 1 mm c) 2 mm and d) 3 mm.

The HPT deformed microstructure of the Cu-matrix at a radius of 3 mm of the compositions $\text{Cu}_{80}(\text{Fe}_{0.7}\text{Co}_{0.3})_{20}$, $\text{Cu}_{80}(\text{Fe}_{0.5}\text{Co}_{0.5})_{20}$ and $\text{Cu}_{80}(\text{Fe}_{0.3}\text{Co}_{0.7})_{20}$ are shown

in Figure 5 a-c, respectively. It can be seen that in all three samples the achieved grain size is less than 100 nm. Furthermore, there are hardly any differences in the Cu grain size between the different compositions visible.

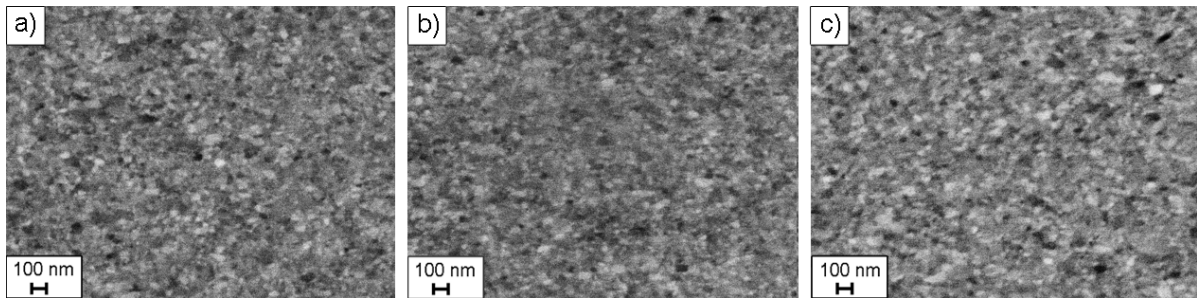


Figure 5: Microstructure of the Cu-matrix of the deformed Cu-Fe-Co samples at a radius of 3 mm: a) $\text{Cu}_{80}(\text{Fe}_{0.7}\text{Co}_{0.3})_{20}$ b) $\text{Cu}_{80}(\text{Fe}_{0.5}\text{Co}_{0.5})_{20}$ and c) $\text{Cu}_{80}(\text{Fe}_{0.3}\text{Co}_{0.7})_{20}$.

In Figure 6 and 7, the BSE micrographs of the second investigated ternary system, Ag-Fe-Co, are shown. Figure 6 illustrates the evolution of the microstructure of the deformed $\text{Ag}_{70}(\text{Fe}_{0.15}\text{Co}_{0.85})_{30}$ sample. The micrographs, taken at a radius of 0, 1, 2, and 3 mm, are representative for all samples that contains 70 at% Ag. The micrographs of the other compositions can be found in the appendix. Figure 7 shows the microstructural evolution of the $\text{Ag}_{50}(\text{Fe}_{0.15}\text{Co}_{0.85})_{50}$ sample.

For all Ag-Fe-Co compositions, which contain 70 at% Ag, remaining particles along the whole radius are visible in the Ag-matrix (Figure 6). In this ternary system, the size of the particles significantly decreases with increasing radius and consequently increasing strain. While at small radii, there are still large particles visible; at a radius of 3 mm there are only numerous small ones observable. Compared to the Cu-Fe-Co samples, it appears that Fe and Co particles are fragmented more homogeneously during the deformation process. However, there is still not enough fragmentation to achieve a complete dissolution. A homogenous single phase microstructure is not obtained at a radius of 3 mm.

The sample with an amount of 50 at% Ag shows a different deformation behaviour (Figure 7). While at a low strain, fragmentation of Fe and Co particles are observed (Figure 7a and b); the sample deforms mainly by shear banding at higher strains. Some shear bands are marked with arrows in Figure 7c and d. It is also visible that the microstructure contains considerably less remaining particles at higher radii for this composition (Figure 7c and d).

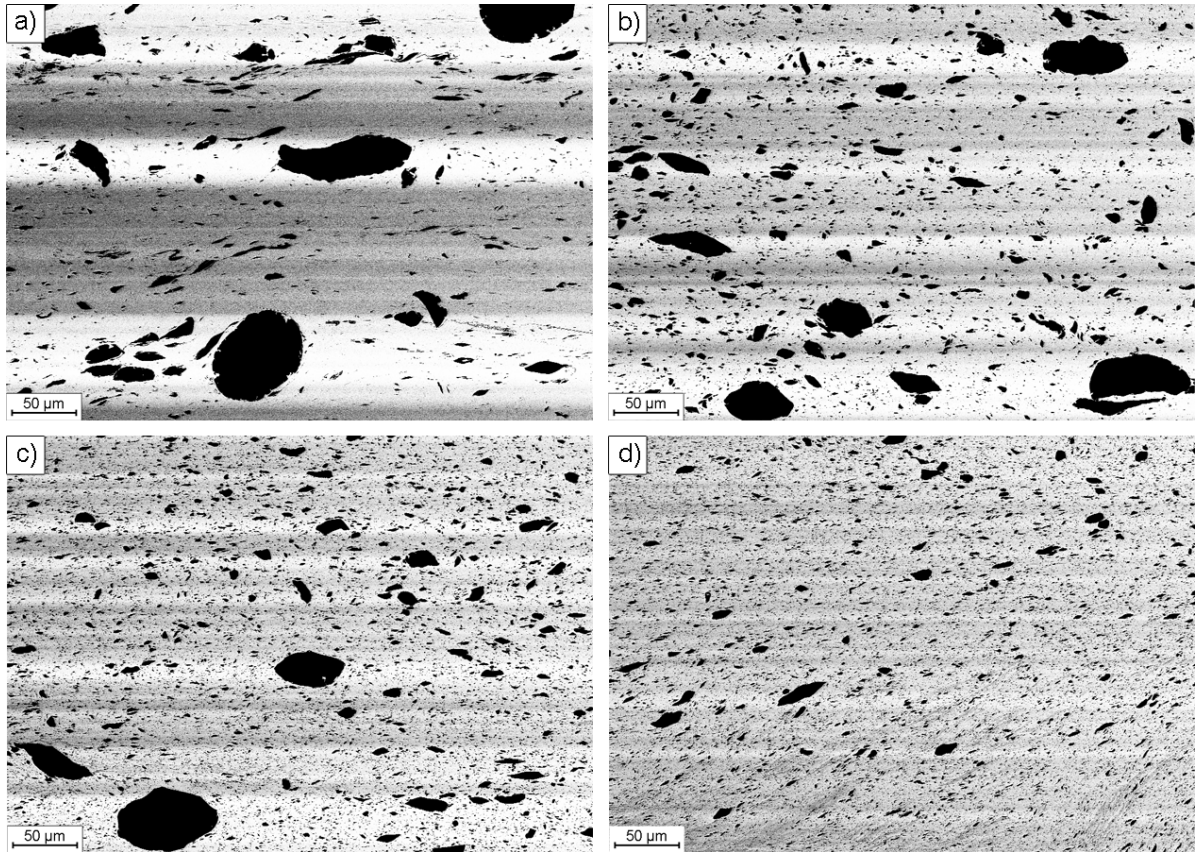


Figure 6: BSE micrographs of the microstructure of the HPT deformed $\text{Ag}_{70}(\text{Fe}_{0.15}\text{Co}_{0.85})_{30}$ sample, taken at a radius of a) 0 mm b) 1 mm c) 2 mm and d) 3 mm.

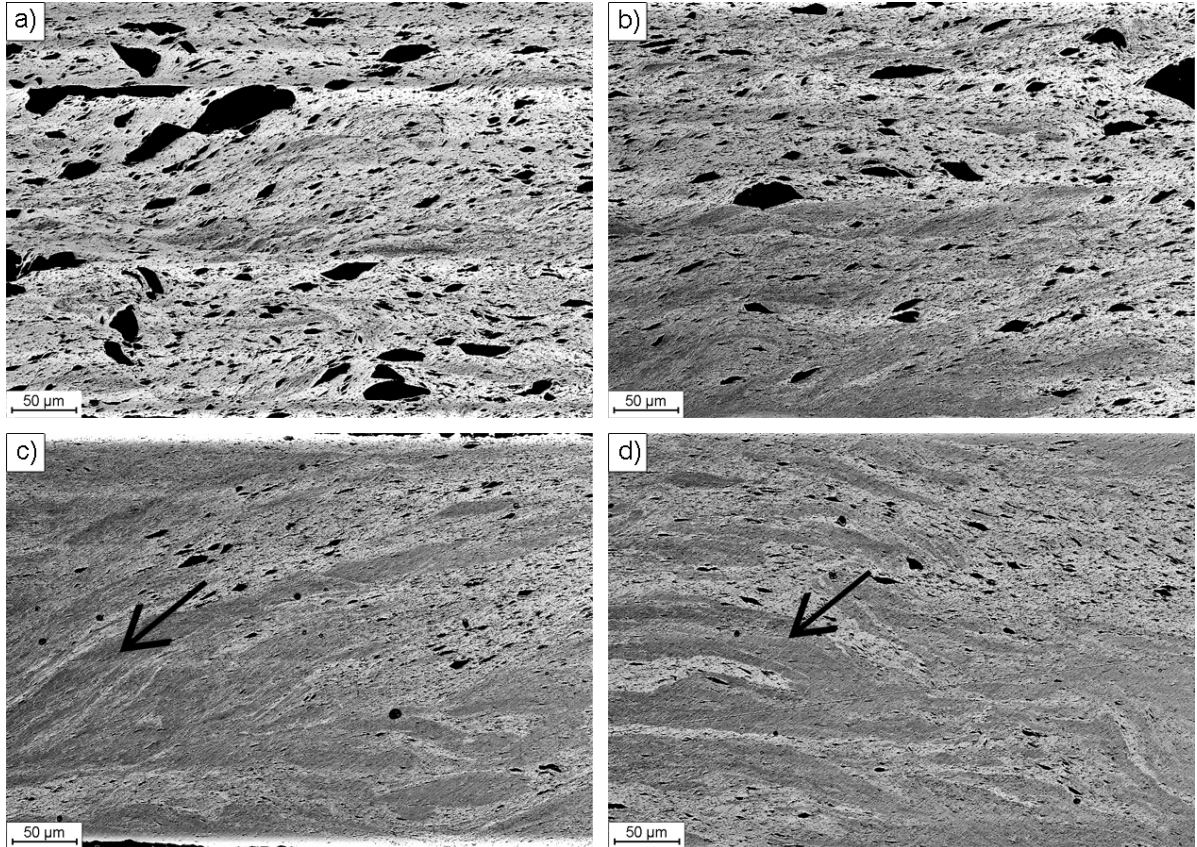


Figure 7: Evolution of the microstructure of the deformed $\text{Ag}_{50}(\text{Fe}_{0.15}\text{Co}_{0.85})_{50}$ sample. BSE micrographs were taken at a radius of a) 0 mm b) 1 mm c) 2 mm and d) 3 mm.

The HPT deformed microstructure of the Ag-matrix of the compositions $\text{Ag}_{70}(\text{Fe}_{0.15}\text{Co}_{0.85})_{30}$, $\text{Ag}_{70}(\text{Fe}_{0.3}\text{Co}_{0.7})_{30}$ and $\text{Ag}_{70}(\text{Fe}_{0.5}\text{Co}_{0.5})_{30}$ are shown in Figure 8a-c, respectively. Figure 8d shows the Ag-matrix of the $\text{Ag}_{50}(\text{Fe}_{0.15}\text{Co}_{0.85})_{50}$ sample. Similar to the samples of the Cu-Fe-Co system, the grain sizes are below 100 nm with hardly any difference in size between the different compositions.

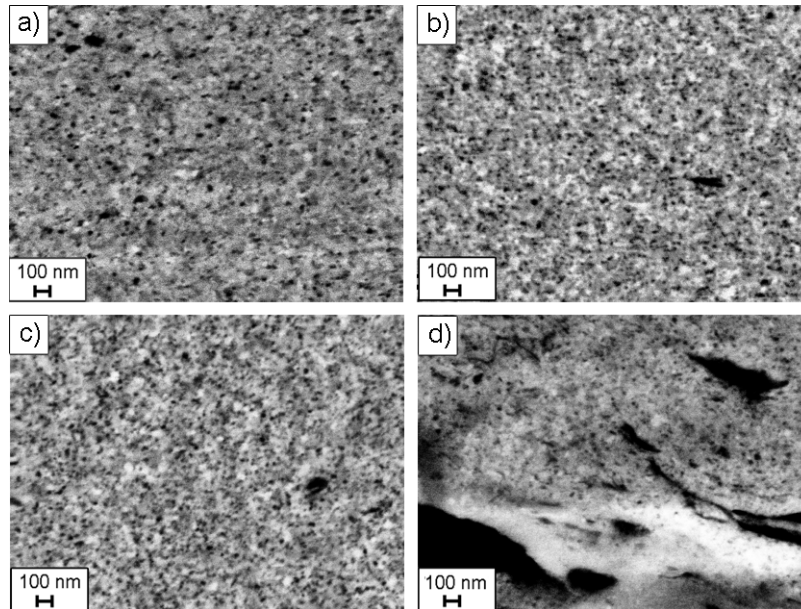


Figure 8: Microstructure of the Ag-matrix of the deformed Ag-Fe-Co samples at a radius of 3 mm: a) $\text{Ag}_{70}(\text{Fe}_{0.15}\text{Co}_{0.85})_{30}$ b) $\text{Ag}_{70}(\text{Fe}_{0.3}\text{Co}_{0.7})_{30}$ c) $\text{Ag}_{70}(\text{Fe}_{0.5}\text{Co}_{0.5})_{30}$ and d) $\text{Ag}_{50}(\text{Fe}_{0.15}\text{Co}_{0.85})_{50}$.

4.2. Influence of an initial annealing treatment on structural evolution

To study the influence of an initial annealing treatment on the deformation behaviour, the compositions $\text{Cu}_{80}(\text{Fe}_{0.5}\text{Co}_{0.5})_{20}$ and $\text{Ag}_{70}(\text{Fe}_{0.15}\text{Co}_{0.85})_{30}$ were chosen. The aim of the annealing treatment was to generate a coarser microstructure in the consolidated Co and Fe phases to obtain similar hardness as the Cu or Ag matrix. Thus, a better co-deformation might occur during the subsequent HPT deformation.

The precompacted and at 500°C for 60 minutes isothermally annealed microstructure of the $\text{Cu}_{80}(\text{Fe}_{0.5}\text{Co}_{0.5})_{20}$ sample is shown in Figure 9a. EDX measurements were done to differentiate the various phases in the composite. The spherical particle on the left side in the micrograph is Co; the elongated particles are Fe. One can see that the annealing treatment effected grain growth of the Cu-matrix and the Fe particles. However, the microstructure of the Co particle hardly changed, so that its grain size remained small. A magnified micrograph of the Co microstructure is shown in Figure 9b.

The annealing treatment at 600°C for 30 minutes on the precompacted $\text{Cu}_{80}(\text{Fe}_{0.5}\text{Co}_{0.5})_{20}$ sample led to significant grain growth in the Fe phase, and the

grain size of the Cu phase increased as well. The micrograph of the annealed microstructure is shown in Figure 10a. Figure 10b displays the magnified microstructure of a Co particle after the annealing treatment. The microstructure of the Co particle is similar to the one obtained after annealing at 500°C for 60 minutes.

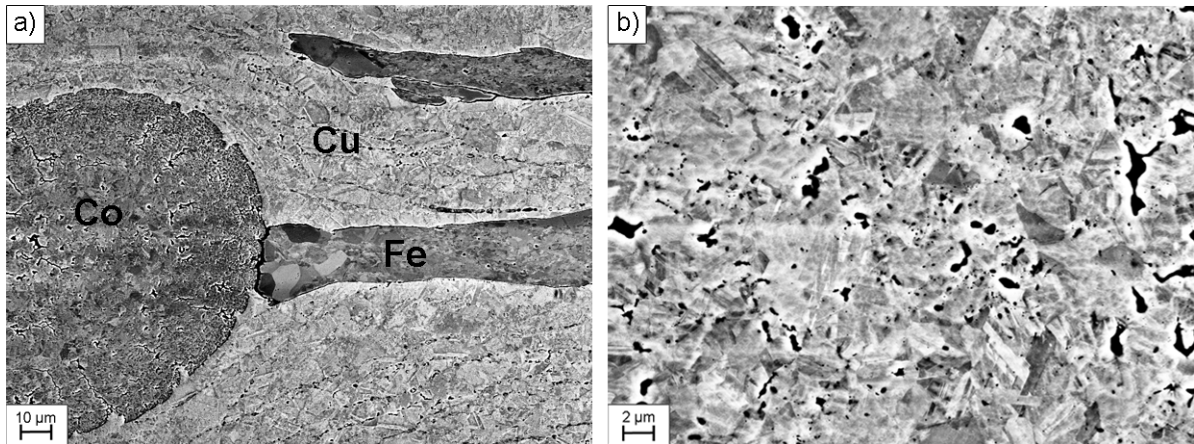


Figure 9: a) Microstructure of the $\text{Cu}_{80}(\text{Fe}_{0.5}\text{Co}_{0.5})_{20}$ sample after annealing for 60 minutes at 500°C. b) Magnified image of a Co particle after the annealing treatment.

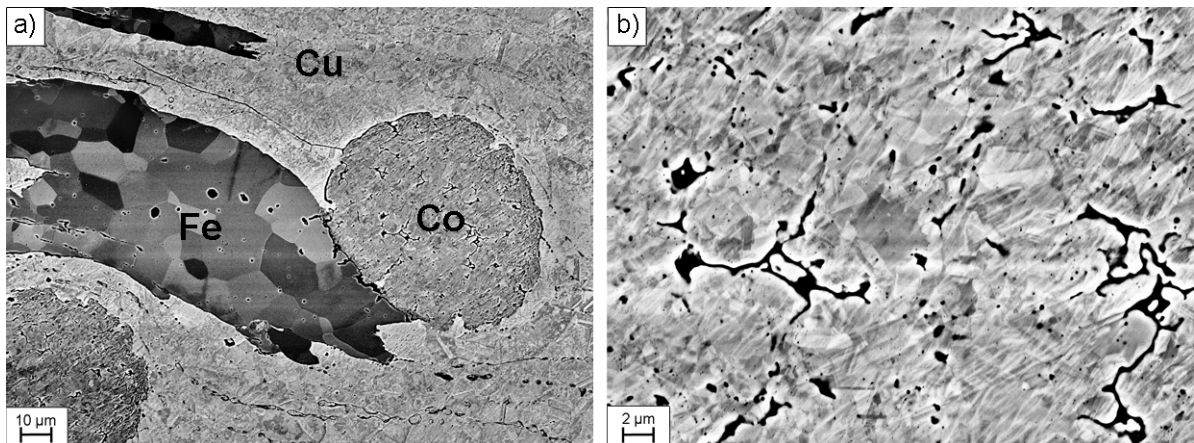


Figure 10: a) Microstructure of the $\text{Cu}_{80}(\text{Fe}_{0.5}\text{Co}_{0.5})_{20}$ sample after annealing for 30 minutes at 600°C. b) Magnified image of a Co particle after the annealing treatment.

One sample of the selected composition $\text{Ag}_{70}(\text{Fe}_{0.15}\text{Co}_{0.85})_{30}$ was also isothermally annealed at 500°C for 60 minutes after the consolidation process. The annealed microstructure of the sample is shown in Figure 11a. Due to the similar shape of the particles as in the Cu-Fe-Co samples, Co and Fe particles can be identified easily. The microstructure of the various phases are shown in Figure 11a. In this micrograph, it is clearly visible that in the Fe phase pronounced grain growth took place during the annealing treatment. A microstructure of a Co particle is shown in Figure 11b. Also in this case, the microstructure of the Co phases is almost unchanged.

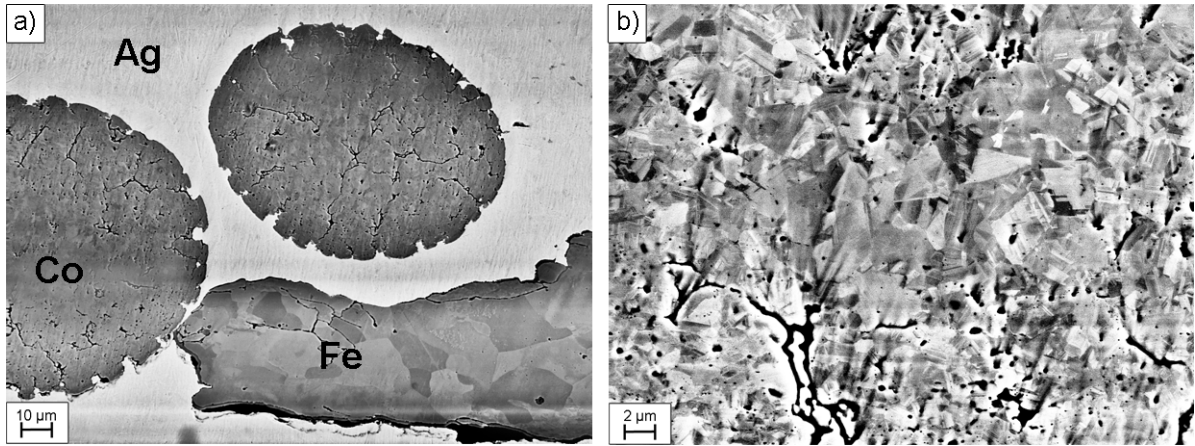


Figure 11: a) Microstructure of the Ag₇₀(Fe_{0.15}Co_{0.85})₃₀ sample after annealing for 60 minutes at 500°C. b) Microstructure of a Co particle after the annealing treatment.

Additionally microhardness measurements in the individual phases were carried out to investigate the change in hardness, which took place during the different annealing treatments. Table 3 lists the averaged hardness values (HV0.05) of the different phases in the various Cu₈₀(Fe_{0.5}Co_{0.5})₂₀ and Ag₇₀(Fe_{0.15}Co_{0.85})₃₀ samples. One can see that the annealing treatments led in each case to a strong softening of the Cu and Fe phase. The hardness of the Co particles is hardly changed during annealing, which corresponds quite well to the microstructural observations of the Co-phase after annealing.

	only precompacted	precompacted and annealed at 600°C for 30 minutes	precompacted and annealed at 500°C for 60 minutes	precompacted and annealed at 600°C for 120 minutes
Cu-Fe-Co				
Co	291 ± 7	215 ± 18	226 ± 6	222 ± 14
Fe	146 ± 5	83 ± 1		
Cu	120 ± 5	39 ± 3	38 ± 1	
Ag-Fe-Co				
Co	282 ± 7	202 ± 10		
Fe	151 ± 6	68 ± 5		
Ag	81 ± 1	34 ± 2		

Table 3: Hardness (HV0.05) of the Co particles, the Fe particles and the Cu- and Ag-matrix after various annealing treatments in the Cu₈₀(Fe_{0.5}Co_{0.5})₂₀ and Ag₇₀(Fe_{0.15}Co_{0.85})₃₀ samples.

Figure 12 displays the microstructural evolution of the HPT deformed Cu₈₀(Fe_{0.5}Co_{0.5})₂₀ sample, which was previously annealed at 500°C for 60 minutes. The BSE micrographs were taken again at a radius of 0, 1, 2, and 3 mm. Compared to the evolution of the microstructure of the un-annealed Cu₈₀(Fe_{0.5}Co_{0.5})₂₀ sample (Figure 4), the annealing treatment induces no big change of the deformation

behaviour. Again, at every radial position, there are still particles remaining. As in the un-annealed sample, the particles at a radius of 3 mm are relatively large, and the density of the particles decreases along the radius. The microstructural evolution of the HPT deformed $\text{Cu}_{80}(\text{Fe}_{0.5}\text{Co}_{0.5})_{20}$ sample, which was annealed at 600°C for 30 minutes before deformation, is quite similar to the evolution shown in Figure 12 and can be found in the appendix.

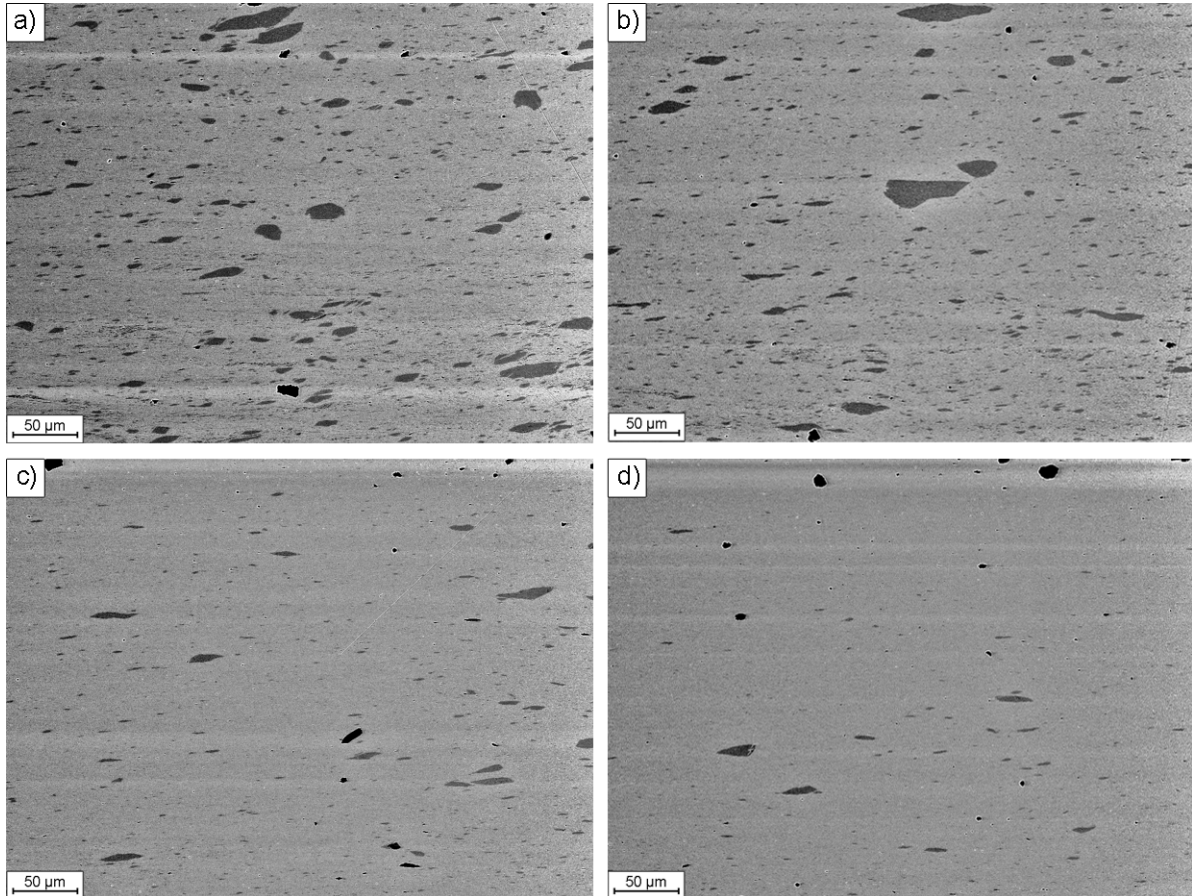


Figure 12: Microstructural evolution of the annealed (500°C , 60 minutes) and HPT deformed $\text{Cu}_{80}(\text{Fe}_{0.5}\text{Co}_{0.5})_{20}$ sample at a radius of a) 0 mm b) 1 mm c) 2 mm and d) 3 mm.

BSE micrographs of the microstructure of the Cu-matrix of the different $\text{Cu}_{80}(\text{Fe}_{0.5}\text{Co}_{0.5})_{20}$ samples at a radius of 3 mm are compared in Figure 13. It is obvious, that the Cu-matrix of the un-annealed sample (Figure 13a) and the annealed samples (Figure 13b and c) have nearly the same grain size after the deformation process.

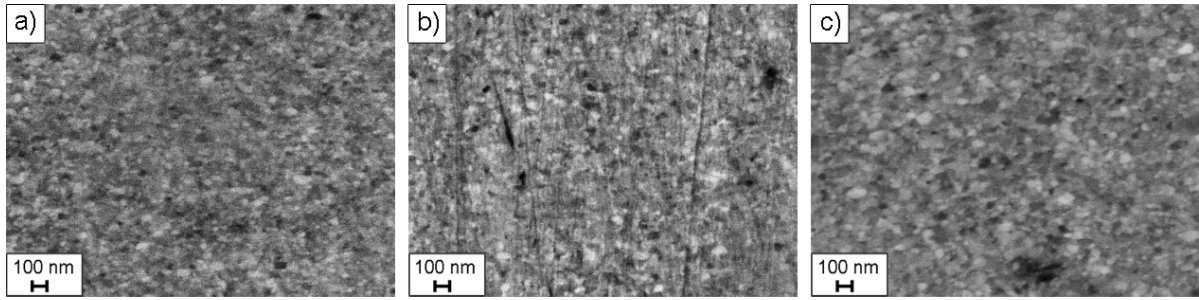


Figure 13: Microstructure of the Cu-matrix of the deformed $\text{Cu}_{80}(\text{Fe}_{0.5}\text{Co}_{0.5})_{20}$ samples at a radius of 3 mm: a) un-annealed sample b) annealed at 500°C for 60 minutes and c) annealed at 600°C for 30 minutes.

The microstructural evolution of the deformed $\text{Ag}_{70}(\text{Fe}_{0.15}\text{Co}_{0.85})_{30}$ sample, which was annealed at 500°C for 60 minutes before the HPT deformation, is shown in Figure 14. For this composition, the annealing treatment does not influence the deformation behaviour as well. Similar to all other investigated samples, particles are present along the radius. Even at a radius of 3 mm, there are relatively large particles visible. In comparison to the un-annealed $\text{Ag}_{70}(\text{Fe}_{0.15}\text{Co}_{0.85})_{30}$ sample (Figure 6), the previously annealed sample contains much more large particles at a radius of 3 mm (Figure 14d). However, the size of most of the particles decreases with increasing radius and strain.

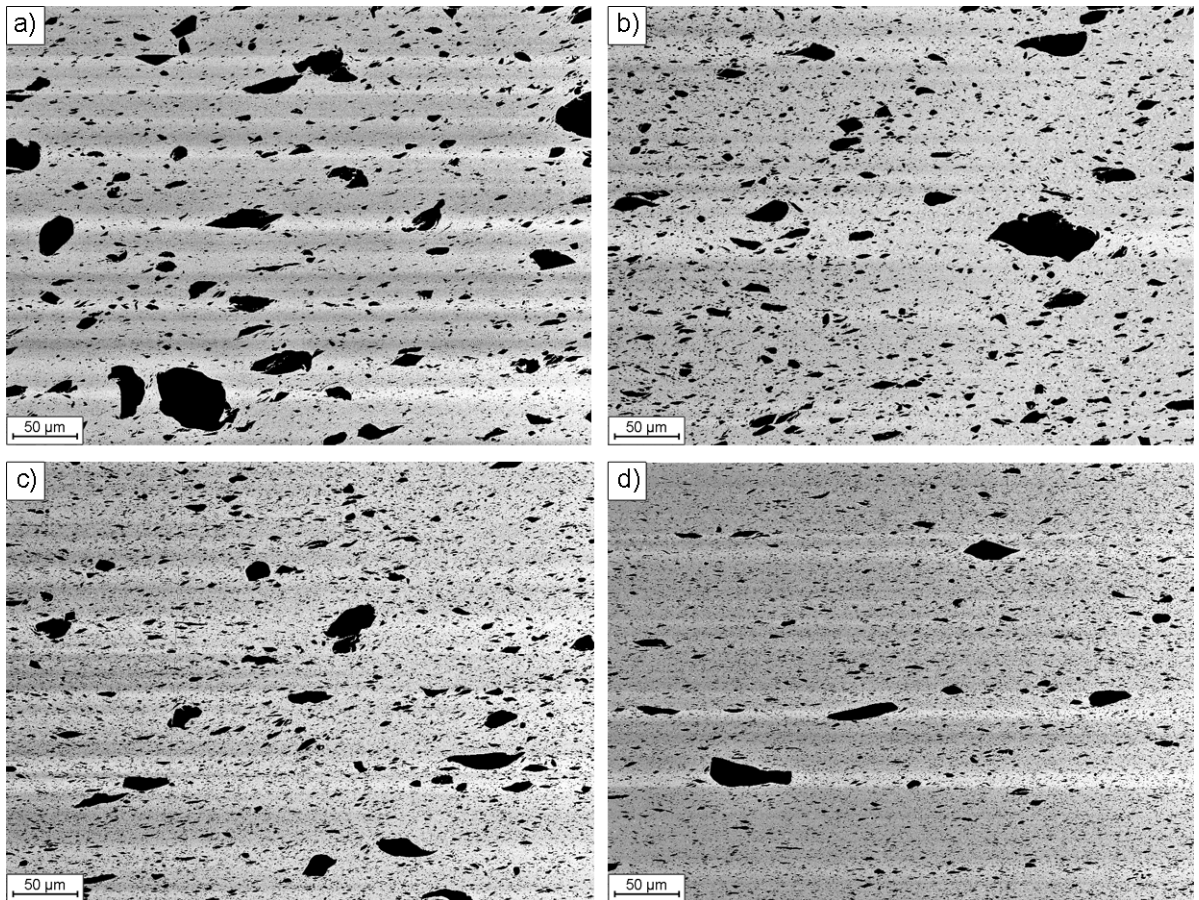


Figure 14: Microstructural evolution of the annealed (500°C , 60 minutes) and HPT deformed $\text{Ag}_{70}(\text{Fe}_{0.15}\text{Co}_{0.85})_{30}$ sample at a radius of a) 0 mm b) 1 mm c) 2 mm and d) 3 mm.

Figure 15 shows the BSE micrographs of the microstructure of the Ag-matrix at a radius of 3 mm of the deformed $\text{Ag}_{70}(\text{Fe}_{0.15}\text{Co}_{0.85})_{30}$ sample without (Figure 15a) and with (Figure 15b) previous annealing treatment. There is hardly any difference between the microstructures of the Ag-matrix visible.

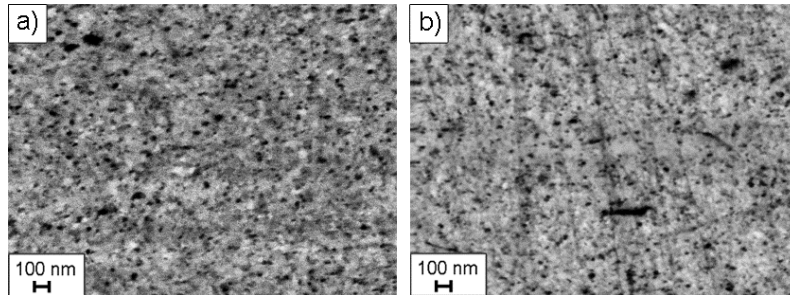


Figure 15: Microstructure of the Ag-matrix at a radius of 3 mm of the deformed $\text{Ag}_{70}(\text{Fe}_{0.15}\text{Co}_{0.85})_{30}$ samples: a) without annealing treatment, b) with annealing at 500°C for 60 minutes before HPT deformation.

4.3. Phase Analysis with ImageJ

Phase analyses were carried out to obtain a better understanding of the deformation behaviour and also the influence of the initial state of the composites on it. For every sample, un-annealed and annealed ones, analyses were performed at a radius of 0, 1, 2, and 3 mm. The results of the phase analyses of one sample are summarized in a histogram displaying the number of particles for different ranges of feret diameter at different radii. In this section, histograms of selected samples, which are representatively for the others, are shown. All other histograms can be found in the appendix.

Figure 16a exemplary displays the light optical micrograph of the un-annealed and deformed $\text{Cu}_{80}(\text{Fe}_{0.5}\text{Co}_{0.5})_{20}$ sample at a radius of 0 mm. The corresponding processed image, where the detected particles are bordered with lines, is shown in Figure 16b. All bordered particles in Figure 16b were quantified by ImageJ, and the feret diameters of the particles were calculated.

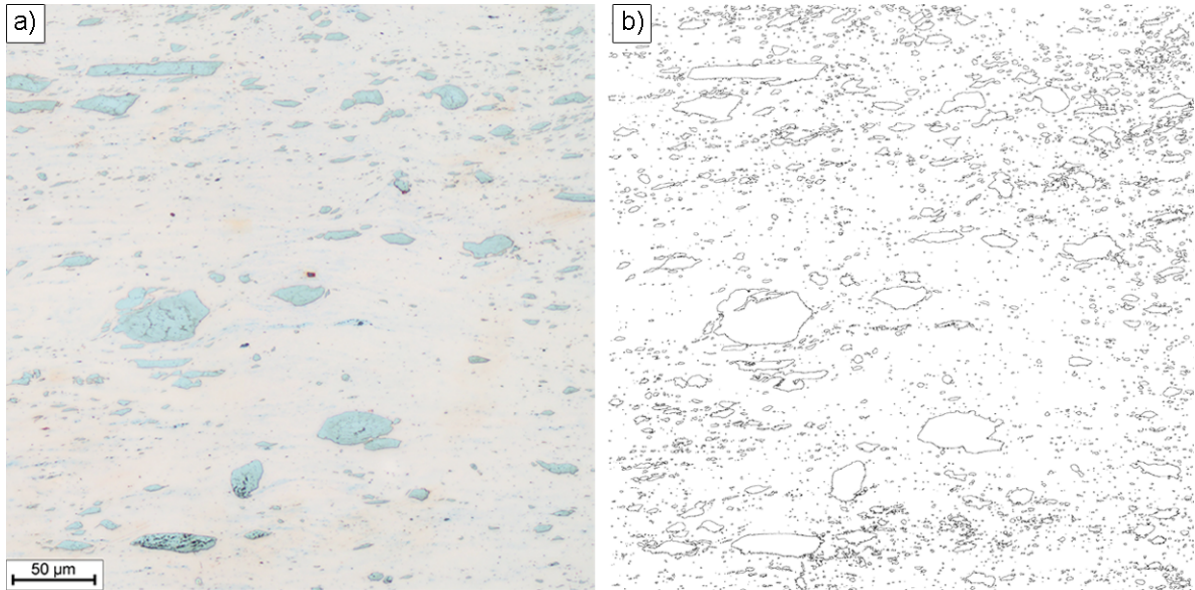


Figure 16: Images for the phase analysis of the un-annealed and deformed $\text{Cu}_{80}(\text{Fe}_{0.5}\text{Co}_{0.5})_{20}$ sample at a radius of 0 mm: a) light optical micrographs, b) the corresponding image with the bordered particles.

The results of the phase analyses of the deformed $\text{Cu}_{80}(\text{Fe}_{0.5}\text{Co}_{0.5})_{20}$ samples are shown in Figure 17. The histogram displays how many particles with a categorized feret diameter were detected along each radius. The histogram of the $\text{Cu}_{80}(\text{Fe}_{0.5}\text{Co}_{0.5})_{20}$ sample without previous annealing treatment (Figure 17a) shows that the number of small particles with a feret diameter less than $10\ \mu\text{m}$ decreases with increasing radius or rather increasing strain. At a radius of 3 mm there are significantly less remaining particles in each category compared to the other analysed positions of this sample. The other compositions of this ternary system show the same characteristic.

Figure 17b shows the results of the phase analyses of the previous at 500°C for 60 minutes annealed $\text{Cu}_{80}(\text{Fe}_{0.5}\text{Co}_{0.5})_{20}$ sample. Again, the particle density decrease with increasing radius. However, compared to the un-annealed $\text{Cu}_{80}(\text{Fe}_{0.5}\text{Co}_{0.5})_{20}$ sample, much more particles, which are smaller than $10\ \mu\text{m}$, are embedded in the matrix.

For the un-annealed and deformed $\text{Cu}_{80}(\text{Fe}_{0.5}\text{Co}_{0.5})_{20}$ sample, the largest particle at 0 mm has a feret diameter of $84\ \mu\text{m}$. Since the resulting shear strain at this position is theoretically zero, the size of this particle is taken as the maximum value of the initial size d_0 of this volume element. According to Equation (3), the final size d_{HPT} of the largest particle at a radius of 3 mm, where the applied strain is 2356, should be 36 nm. However, the feret diameter of the largest particle at a radius of 3 mm is 10^3 times larger ($54\ \mu\text{m}$) than this theoretical value.

The feret diameter of the largest particle at a radius of 0 mm in the previous at 500°C for 60 minutes annealed $\text{Cu}_{80}(\text{Fe}_{0.5}\text{Co}_{0.5})_{20}$ sample is 81 μm , which is similar to d_0 of the un-annealed sample. Since the results of the analysis at a radius of 3 mm show that the largest particle is still 32 μm , the actual final size of that volume element does not reach the theoretical value d_{HPT} as well. Table 4 lists the feret diameters of the largest particles detected at a radius of 0 mm and 3 mm for all samples in the investigated Cu-Fe-Co system.

The amount of large particles, which have a feret diameter larger than 10 μm or 5 μm and are detected at a radius of 3 mm, is quite similar for all three different Cu-Fe-Co compositions. The result of this evaluation is also shown in Table 4. Between the un-annealed and annealed samples of the composition $\text{Cu}_{80}(\text{Fe}_{0.5}\text{Co}_{0.5})_{20}$, there are no big differences in the number of particles, which are larger than 10 μm . However, it is ascertainable that in the 600°C annealed $\text{Cu}_{80}(\text{Fe}_{0.5}\text{Co}_{0.5})_{20}$ sample much more remaining particles with a feret diameter larger than 5 μm are present.

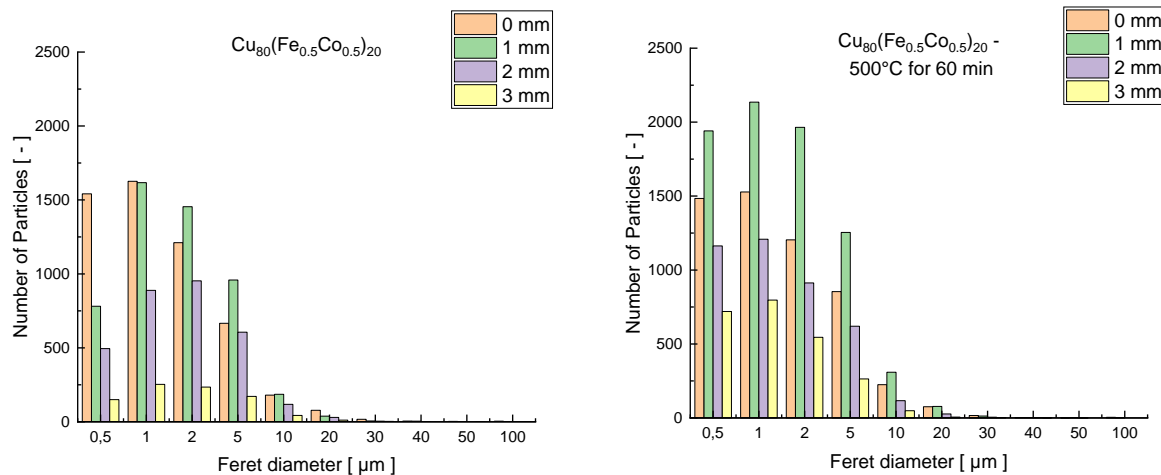


Figure 17: Results of the phase analyses of the deformed $\text{Cu}_{80}(\text{Fe}_{0.5}\text{Co}_{0.5})_{20}$ samples along the radius: a) without previous annealing treatment and b) with annealing at 500°C for 60 minutes.

	Largest particle at r = 0 mm d ₀ [μm]	Largest particle at r = 3 mm [μm]	# particles >10 μm at r = 3 mm	# particles > 5 μm at r = 3 mm
Cu ₈₀ (Fe _{0.7} Co _{0.3}) ₂₀	57	32	7	41
Cu ₈₀ (Fe _{0.5} Co _{0.5}) ₂₀	84	54	16	59
Cu ₈₀ (Fe _{0.3} Co _{0.7}) ₂₀	86	20	13	62
Cu ₈₀ (Fe _{0.5} Co _{0.5}) ₂₀ 500°C 60 minutes	81	32	10	59
Cu ₈₀ (Fe _{0.5} Co _{0.5}) ₂₀ 600°C 30 min	146	44	24	110

Table 4: Quantitative evaluations of the phase analyses of the various samples of the Cu-Fe-Co system.

The phase analyses along the radius of the Ag₇₀(Fe_{0.15}Co_{0.85})₃₀ sample proves that the evolution of the microstructure is different compared to the Cu-Fe-Co system. In the un-annealed Ag₇₀(Fe_{0.15}Co_{0.85})₃₀ sample the number of particles increase with increasing radius (Figure 18a). Compared to the un-annealed Cu₈₀(Fe_{0.5}Co_{0.5})₂₀ sample (Figure 17a), the number of the remaining particles at a radius of 3 mm is significantly higher.

In the case of the previous annealed Ag₇₀(Fe_{0.15}Co_{0.85})₃₀ sample, the results of the analyses show the same characteristic as the un-annealed sample. The total number of small particles is, compared to the annealed Cu-Fe-Co samples, significantly higher.

The calculated feret diameter of the largest particle, detected at a radius of 0 mm in the Ag₇₀(Fe_{0.15}Co_{0.85})₃₀ sample, is 84 μm. As well as for the samples of the Cu-Fe-Co system, ideal co-deformation did not take place, and the theoretical value for the final size after a shear strain of 2356 (d_{HPT} = 36 nm) is not achieved. The actual feret diameter of the largest particle at a radius of 3 mm is 44 μm. For the annealed Ag₇₀(Fe_{0.15}Co_{0.85})₃₀ sample the largest particles are 96 μm (r = 0 mm) and 36 μm (r = 3 mm).

Table 5 gives detailed information of the results, which were obtained during the phase analyses of the investigated samples of the Ag-Fe-Co system.

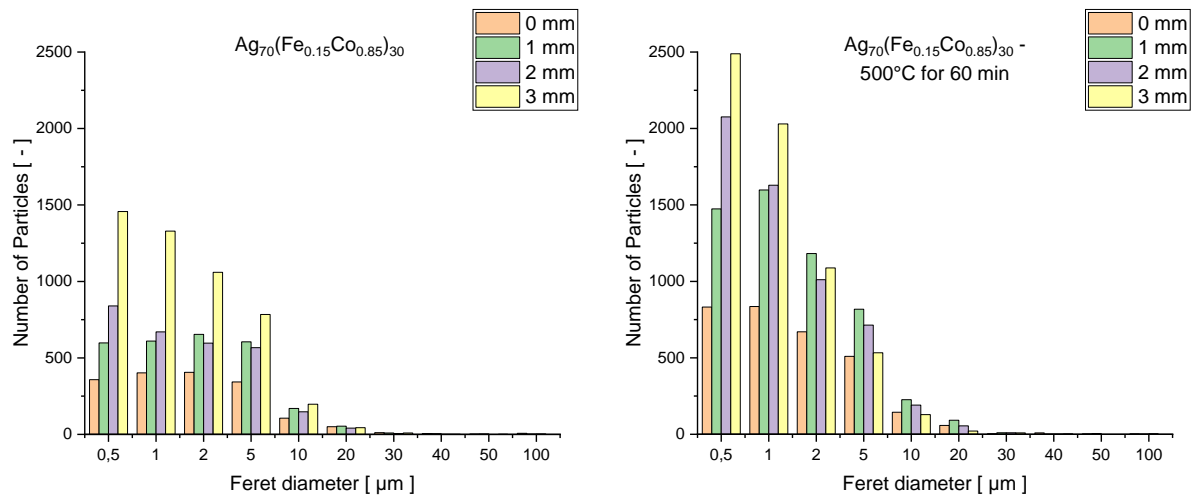


Figure 18: Results of the phase analyses of the deformed $\text{Ag}_{70}(\text{Fe}_{0.15}\text{Co}_{0.85})_{30}$ samples: a) without previous annealing and b) with annealing at 500°C for 30 minutes.

	Largest particle at $r = 0 \text{ mm}$ $d_0 [\mu\text{m}]$	Largest particle at $r = 3 \text{ mm}$ $[\mu\text{m}]$	# particles $> 10 \mu\text{m}$ at $r = 3 \text{ mm}$	# particles $> 5 \mu\text{m}$ at $r = 3 \text{ mm}$
$\text{Ag}_{70}(\text{Fe}_{0.15}\text{Co}_{0.85})_{30}$	84	44	55	252
$\text{Ag}_{70}(\text{Fe}_{0.3}\text{Co}_{0.7})_{30}$	152	100	37	185
$\text{Ag}_{70}(\text{Fe}_{0.5}\text{Co}_{0.5})_{30}$	88	37	7	39
$\text{Ag}_{70}(\text{Fe}_{0.15}\text{Co}_{0.85})_{30}$ 500°C 60 minutes	96	36	32	161
$\text{Ag}_{50}(\text{Fe}_{0.15}\text{Co}_{0.85})_{50}$	162	11	2	21

Table 5: Quantitative evaluations of the phase analyses of the various samples of the Ag-Fe-Co system.

The number of remaining particles in the $\text{Ag}_{50}(\text{Fe}_{0.15}\text{Co}_{0.85})_{50}$ sample are displayed in Figure 19. While at a radius of 0, 1, and 2 mm, the number of small particles is very high; at a radius of 3 mm there are significant less particles left. It is also visible that the number of particles decreases with increasing radius in every category. As mentioned above, this sample shows a different deformation behaviour compared to the other samples of the Ag-Fe-Co system; the results of the phase analyses confirmed this. As shown in Table 5, the fragmentation and dissolution of the particles is massive compared to the samples that contain more Ag. The largest particle at a radius of 0 mm has a feret diameter of $162 \mu\text{m}$; at a radius of 3 mm there are only 2 remaining particles with a diameter larger than $10 \mu\text{m}$. However, the theoretical value of the final size of the particles after the applied shear strain of 2356 ($d_{\text{HPT}} = 69 \text{ nm}$) is also not achieved.

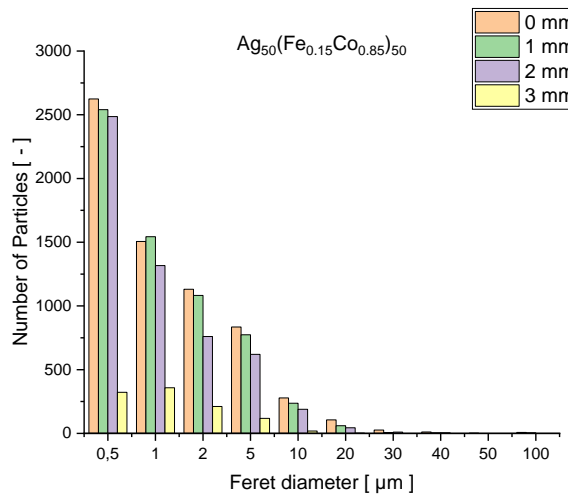


Figure 19: Results of the phase analyses of the deformed $\text{Ag}_{50}(\text{Fe}_{0.15}\text{Co}_{0.85})_{50}$ sample.

Chemical phase analyses with EDX

EDX measurements were done to identify the different phases and to get a rough assessment of how much Fe and Co are dissolved in the Cu- or Ag-matrix, respectively. Furthermore, the influence of the annealing treatment on the dissolution of Fe and Co after HPT deformation should be determined more accurately. Since the measurements give information about the chemical composition in percent by weight (wt%), Table 6 lists the ideal compositions of the investigated $\text{Cu}_{80}(\text{Fe}_{0.5}\text{Co}_{0.5})_{20}$ and $\text{Ag}_{70}(\text{Fe}_{0.15}\text{Co}_{0.85})_{30}$ samples in wt%. To obtain the actual chemical composition of the samples, EDX measurements were performed as area scans at a radius of 3 mm over an area of approximately $300 \times 400 \mu\text{m}^2$. The results of these measurements are listed in Table 6 as well.

Further EDX measurements were carried out at different radii on remaining particles to characterise if the particles are Fe, Co, or a Fe-Co alloy and as spots in the matrix to determine the amount of the solved elements at this position. One example of an EDX spot measurement to investigate the composition of the matrix is shown in Figure 20. Along the radius, more precisely at a radius of 0, 1, 2, and 3 mm, the chemical composition of the matrix was determined three times at each radius and different positions.

$\text{Cu}_{80}(\text{Fe}_{0.5}\text{Co}_{0.5})_{20}$		un-annealed	annealed 600°C for 30 minutes
	ideal	actual measured at 3 mm	actual measured at 3 mm
Cu	81.5	83.3	84.0
Fe	9.0	7.5	7.7
Co	9.5	9.2	8.3
$\text{Ag}_{70}(\text{Fe}_{0.15}\text{Co}_{0.85})_{30}$		un-annealed	annealed 500°C for 60 minutes
	ideal	actual measured at 3 mm	actual measured at 3 mm
Ag	81.1	87.6	81.8
Fe	2.7	2.0	2.2
Co	16.2	10.5	16.0

Table 6: Ideal and actual measured chemical compositions in percent by weight (wt%) of the investigated $\text{Cu}_{80}(\text{Fe}_{0.5}\text{Co}_{0.5})_{20}$ and $\text{Ag}_{70}(\text{Fe}_{0.15}\text{Co}_{0.85})_{30}$ samples.

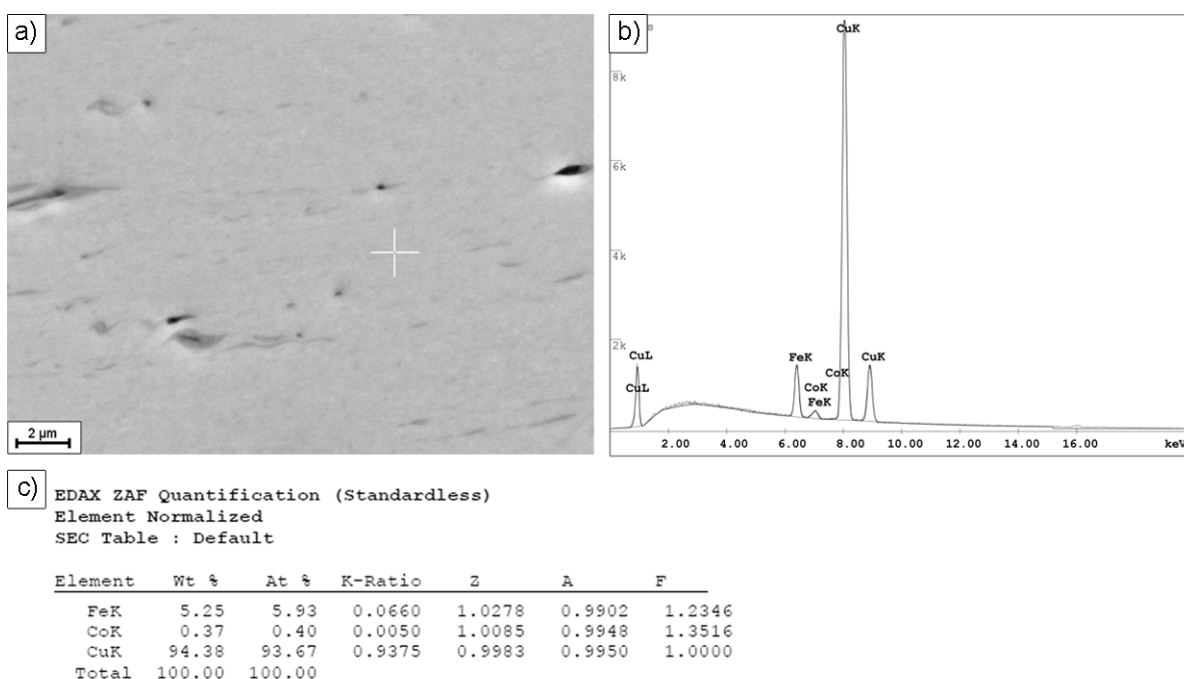


Figure 20: Example of an EDX spot measurement: a) SEM micrograph with the marked spot, where the measurement was carried out, b) the measured EDX spectrum and c) the EDX quantification.

Figure 21 shows a measurement of a Co particle at a radius of 0 mm in the un-annealed $\text{Cu}_{80}(\text{Fe}_{0.5}\text{Co}_{0.5})_{20}$ sample. Because the shape and structure of most of the remaining particles in all samples are very similar to this one, it is assumed that the majority of the remaining particles at higher radii are Co ones.

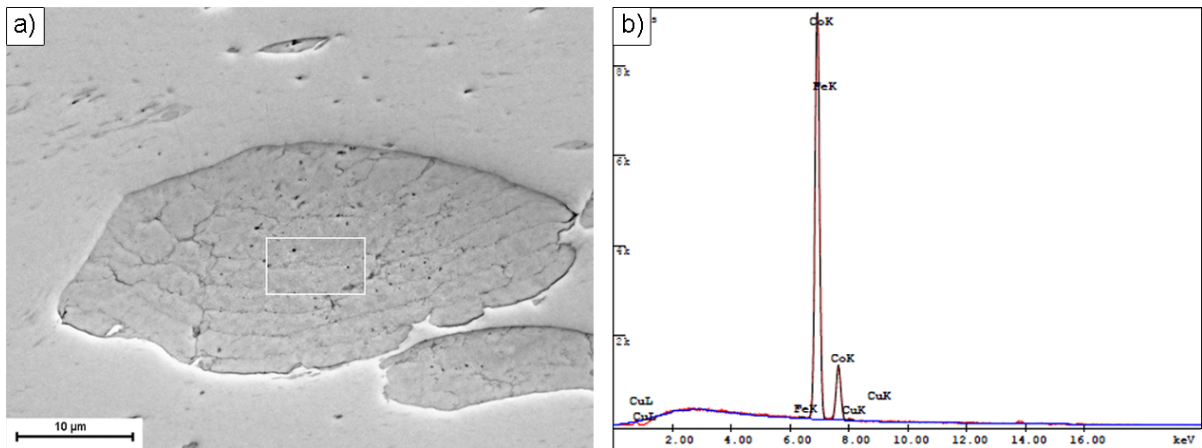


Figure 21: EDX measurement of a Co particle in the deformed $\text{Cu}_{80}(\text{Fe}_{0.5}\text{Co}_{0.5})_{20}$ sample at a radius of 0 mm: a) SEM micrograph with the marked area where the measurements were performed, b) resulting EDX spectrum.

The results of the EDX spot measurements in wt% of the un-annealed and annealed $\text{Cu}_{80}(\text{Fe}_{0.5}\text{Co}_{0.5})_{20}$ sample are shown in Table 7. Hardly any differences are observed between the chemical compositions of the un-annealed and annealed $\text{Cu}_{80}(\text{Fe}_{0.5}\text{Co}_{0.5})_{20}$ samples at a radius of 0 mm. Therefore, only EDX maps, which are shown in Figure 22, of the annealed sample were taken at this radius. In these maps the individual elements, Cu (Figure 22b), Fe (Figure 22c), and Co (Figure 22d), are visualised.

In both investigated $\text{Cu}_{80}(\text{Fe}_{0.5}\text{Co}_{0.5})_{20}$ samples, the amount of Cu decreases with increasing radius, and the amount of the dissolved elements, Fe and Co, increases. This indicates that supersaturated solid solutions were generated to a certain extent during HPT deformation. It can also be observed that the annealing treatment does not affect the dissolving of Fe and Co in the Cu-matrix to a large extent.

Table 8 lists the results of the EDX spot measurements of the un-annealed and annealed $\text{Ag}_{70}(\text{Fe}_{0.15}\text{Co}_{0.85})_{30}$ samples. As well as in the $\text{Cu}_{80}(\text{Fe}_{0.5}\text{Co}_{0.5})_{20}$ samples, the composition changes with increasing radius, and the amount of the dissolved elements, Fe and Co, increases. Furthermore, the amount of Co at a radius of 3 mm is slightly higher in the annealed sample than in the un-annealed one. Figure 23 shows a SEM micrograph and the corresponding EDX maps at a radius of 3 mm of the annealed $\text{Ag}_{70}(\text{Fe}_{0.15}\text{Co}_{0.85})_{30}$ sample. It can be seen in Figure 23c, which illustrates the Fe distribution, that the element is evenly distributed in the matrix. Additionally, these EDX maps give an indication that most of the remaining particles are Co ones (see Figure 23d).

Cu ₈₀ (Fe _{0.5} Co _{0.5}) ₂₀								
	un-annealed				annealed at 600°C for 30 minutes			
	0 mm	1 mm	2 mm	3 mm	0 mm	1 mm	2 mm	3 mm
Spot 1								
Cu	94.4	95.9	87.8	84.7	97.7	92.6	87.1	86.2
Fe	5.3	2.8	6.0	6.7	1.3	5.3	8.8	4.3
Co	0.4	1.3	6.2	8.6	1.0	2.1	4.1	9.5
Spot 2								
Cu	98.4	94.0	88.2	83.7		92.6	87.7	85.3
Fe	1.4	4.0	7.4	6.7		4.7	8.5	8.1
Co	0.2	2.0	4.5	9.6		2.7	3.9	6.6
Spot 3								
Cu	97.2	90.9	87.1	83.4		91.3	87.8	86.8
Fe	1.7	7.7	6.7	7.5		5.3	7.7	7.0
Co	1.0	1.4	6.2	9.1		3.4	4.5	6.3

Table 7: Results of the EDX measurements in wt% of the un-annealed and annealed and deformed Cu₈₀(Fe_{0.5}Co_{0.5})₂₀ sample.

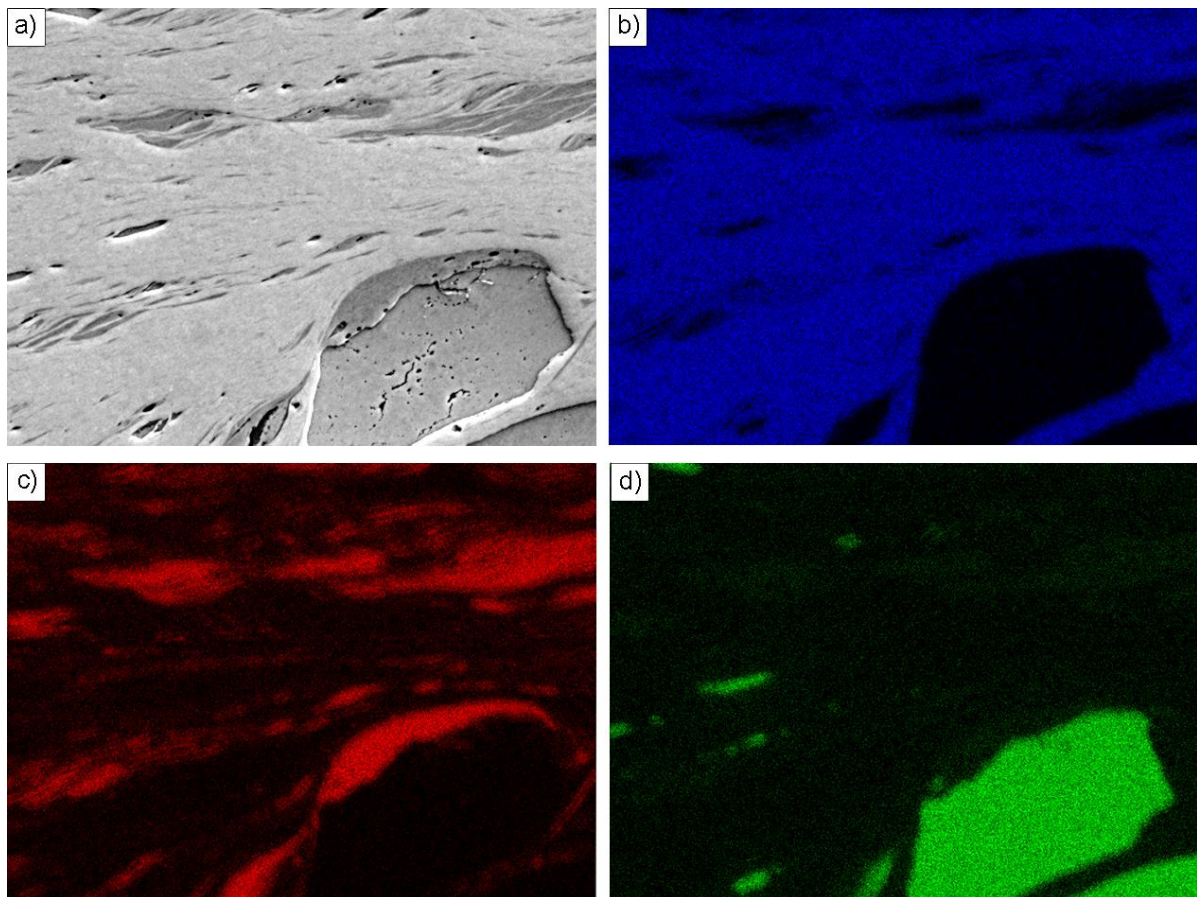


Figure 22: a) SEM micrograph of the annealed and deformed Cu₈₀(Fe_{0.5}Co_{0.5})₂₀ sample at a radius of 0 mm and the corresponding EDX maps of b) Cu c) Fe d) Co.

Ag ₇₀ (Fe _{0.15} Co _{0.85}) ₃₀						
	un-annealed			annealed at 500°C for 60 minutes		
	0 mm	1 mm	3 mm	0 mm	1 mm	3 mm
Spot 1						
Ag	99.4	96.8	91.4	97.6	95.4	91.1
Fe	0.4	2.3	2.6	2.1	3.4	2.5
Co	0.2	0.9	6.1	0.3	1.2	6.3
Spot 2						
Ag	98.9	96.7	94.1	97.5	96.0	91.3
Fe	0.8	2.2	2.4	2.5	2.8	2.3
Co	0.4	1.1	3.6	0.0	1.3	6.5
Spot 3						
Ag	97.9	97.0	92.9	96.9	96.0	92.2
Fe	1.6	2.2	3.0	3.0	2.8	2.3
Co	0.4	0.9	4.1	0.1	1.2	5.5

Table 8: Results of the EDX measurements in wt% of the un-annealed and annealed and deformed Ag₇₀(Fe_{0.15}Co_{0.85})₃₀ sample.

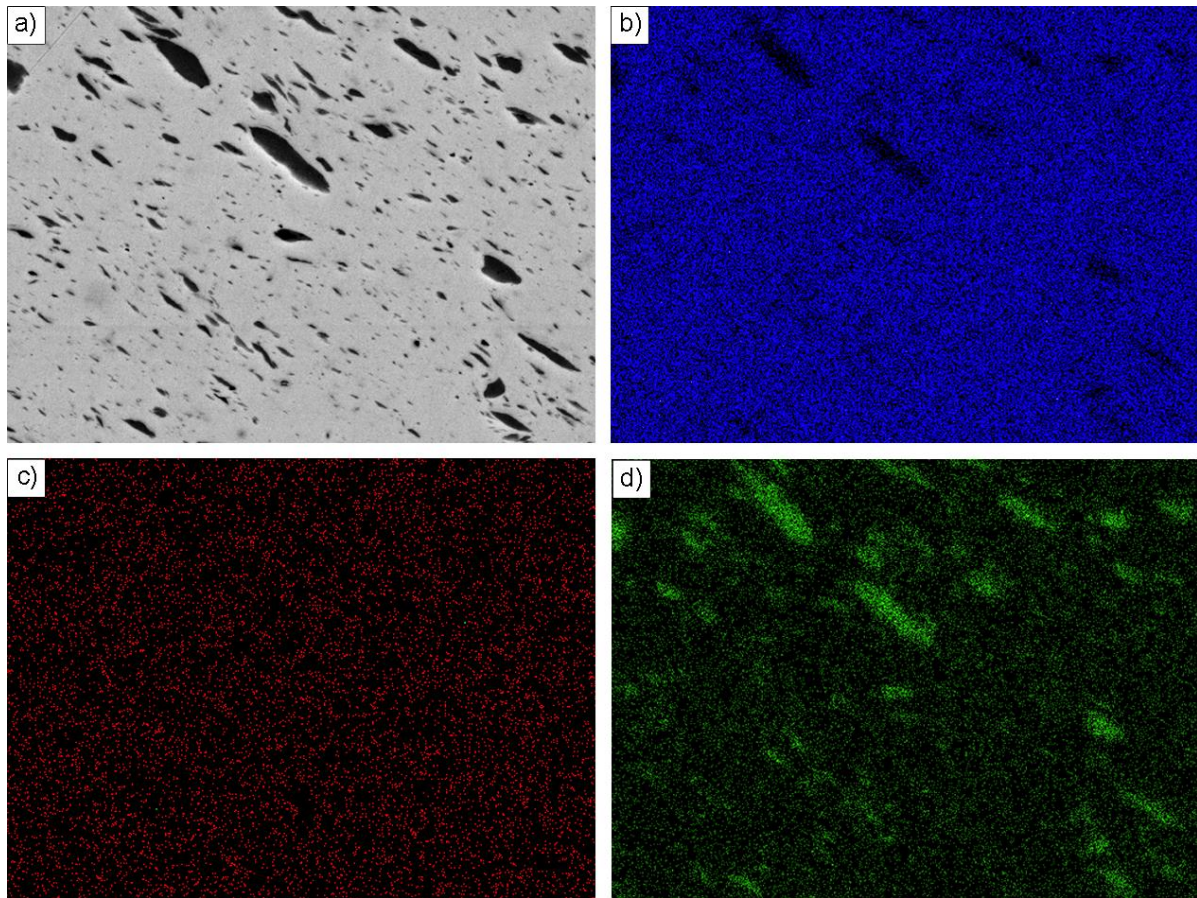


Figure 23: a) SEM micrograph of the annealed and deformed Ag₇₀(Fe_{0.15}Co_{0.85})₃₀ sample at a radius of 3 mm and the corresponding EDX maps of b) Ag c) Fe d) Co.

4.4. Microhardness as function of applied strain

Figure 24 and 25 show the results of the Vickers hardness measurements along the radius of the HPT deformed samples, un-annealed (a) and annealed (b), of both investigated ternary systems.

The microhardness of the samples of the ternary Cu-Fe-Co system is shown in Figure 24. It can be clearly seen that the microhardness of the un-annealed and deformed samples increases with the radius (Figure 24a). The hardness increase is mainly attributed to the decrease of the Cu-matrix grain size and might also be due to the increasing amount of dissolved Fe and Co in the Cu-matrix. Furthermore, the measurements show that for all three compositions the same level of hardness (approximately 310 HV) is achieved at a radius of 3 mm. This corresponds quite well to the similar Cu-matrix grain size of the different samples at this radius (Figure 5).

The determined microhardness of the previous annealed and then HPT deformed $\text{Cu}_{80}(\text{Fe}_{0.5}\text{Co}_{0.5})_{20}$ samples is shown in Figure 24b. The values of the previous annealed samples differ only slightly from the values of the sample without previous annealing treatment. This is consistent with the similarity of the evolution of the microstructure (Figure 12). Furthermore, the microhardness values indicate that the same grain size at a radius of 3 mm in the different samples is achieved, which is also confirmed by SEM (Figure 13).

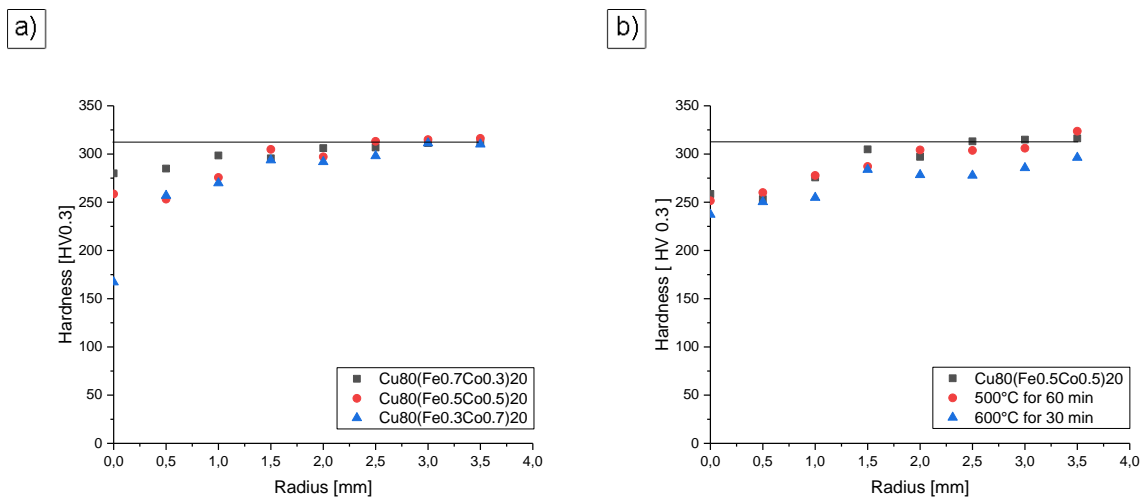


Figure 24: Microhardness measured along the radius of the HPT deformed samples of the investigated Cu-Fe-Co system: a) Results of the different investigated samples without previous annealing treatment, b) Results of the annealed $\text{Cu}_{80}(\text{Fe}_{0.5}\text{Co}_{0.5})_{20}$ samples compared to the un-annealed sample with the same composition.

The microhardness values of the HPT deformed Ag-Fe-Co samples without previous annealing treatment are displayed in Figure 25a. They show a similar hardness evolution as the samples of the Cu-Fe-Co system. For all samples the hardness increases with the radius, whereby the hardness values of the $\text{Ag}_{50}(\text{Fe}_{0.15}\text{Co}_{0.85})_{50}$ sample is generally higher than the ones which contain 70 at% Ag. For the samples containing 70 at% Ag, a final microhardness of approximately 220 HV is reached; the sample containing 50 at% Ag attains a higher microhardness of 300 HV.

For the microhardness of the annealed and HPT deformed $\text{Ag}_{70}(\text{Fe}_{0.15}\text{Co}_{0.85})_{30}$ sample a slightly higher microhardness (hardness difference approximately 30 HV) is observed along the whole radius (Figure 25b).

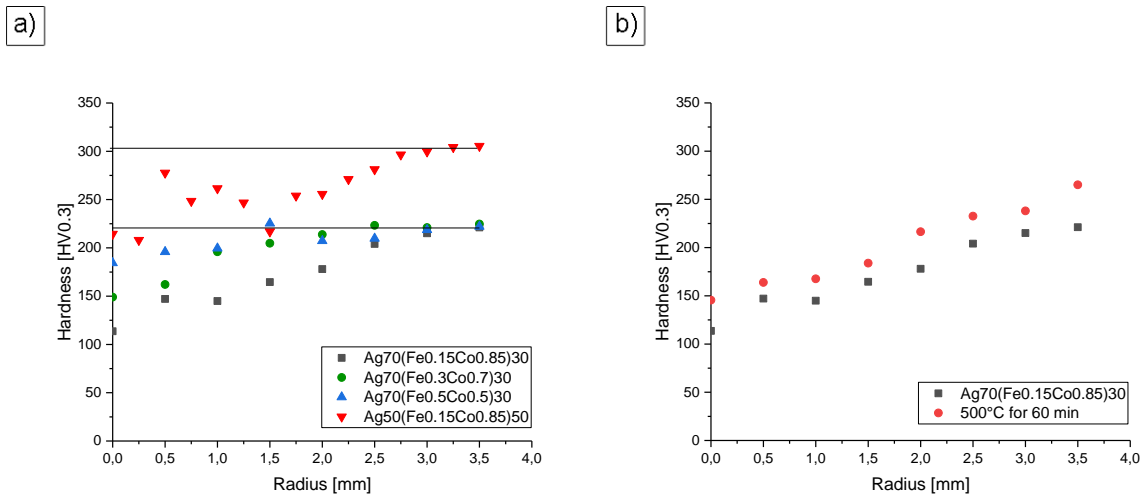


Figure 25: Microhardness measured along the radius of the HPT deformed samples of the investigated Ag-Fe-Co system: a) Un-annealed samples, b) Comparison of the microhardness of the annealed and un-annealed $\text{Ag}_{70}(\text{Fe}_{0.15}\text{Co}_{0.85})_{30}$ samples.

5. Discussion

The initial microhardness of the matrix material of both ternary systems (Cu and Ag) is much lower than the hardness of the Co particles and the hardness of the Fe phase is also higher compared to the Ag-matrix; thus hardly any co-deformation occurs during the HPT deformation process. While in all un-annealed samples a strong plastic deformation of the soft phase takes place, the deformation behaviour of the hard Fe and Co phases is mostly fragmentation by elongation and repeated fracturing. The strong strain localisation in the soft matrix further retards the refinement process of the Co and Fe phase; therefore, in each sample remaining particles can be found along the radii. Particles even occur at a radius of 3 mm, where the applied strain is very high. From EDX measurements, it is assumed that most of the remaining particles are Co particles. Since the hardness difference between the Fe phase and the Cu- and Ag-matrix is less pronounced, the Fe phase deforms to a larger extent which is considered to accelerate the fragmentation and subsequent dissolution of this phase.

The microstructural analyses of the $\text{Ag}_{50}(\text{Fe}_{0.15}\text{Co}_{0.85})_{50}$ sample show that the deformation behaviour is different for this composition. Compared to the other samples, fragmentation of the Fe and Co particles takes place only at low strains. Afterwards, strain localisation in shear bands occurs. At a radius of 3 mm, there are, however, only a few small particles left in the Ag-matrix.

In both ternary systems there are hardly any microstructural differences in the final grain size of the Cu- and Ag-matrices for the different compositions at a radius of 3 mm visible. For each composition, the resulting grain sizes are, however, under 100 nm. The grain size of pure HPT deformed Cu and pure Ag is approximately 180 nm and 250 nm, respectively [19]. A reason for the smaller grain size of the Cu- and Ag-matrices might be strain induced mixing of Fe and Co in the corresponding matrix due to the HPT deformation since the steady state grain size during HPT can be decreased by alloying.

A previous annealing treatment does not significantly influence the deformation behaviour of the investigated samples. After the HPT deformation process, there are still remaining particles at a radius of 3 mm visible for both investigated ternary systems. One reason for the similar deformation behaviour is the minor change of the Co microstructure during annealing as shown by microstructural investigations and hardness measurements. Because the hardness of the Co phase remains almost the same, no improvement of the deformation behaviour of the composite materials takes place. However, the particle analyses show that the annealing

treatment enhances the refinement of the particles. The largest particles at a radius of 3 mm are somewhat smaller, and the amount of remaining particles is higher in the annealed samples.

EDX measurements of the un-annealed and annealed samples show that a partial supersaturated Cu or Ag solid solution might be created, because a certain amount of Co and Fe seems to be dissolved in the matrix material at a radius of 3 mm. The EDX measurements also show that the amount of Co, which is dissolved in the Ag-matrix, is somewhat higher in the annealed $\text{Ag}_{70}(\text{Fe}_{0.15}\text{Co}_{0.85})_{30}$ sample compared to the un-annealed sample with the same composition.

6. Conclusion and Outlook

In this thesis, the deformation behaviour of different compositions of the ternary Cu-Fe-Co and Ag-Fe-Co system was investigated. Additionally, the influence of the initial microstructure of the composite on the microstructural evolution was studied. Therefore, additional annealing treatments were carried out before the HPT deformation as well. The main conclusions of the thesis are following:

- The deformation behaviour of the composites during HPT deformation is mostly fragmentation of the Co and Fe particles in the Cu- or rather Ag-matrix. Hardly any co-deformation took place during the HPT deformation process.
- Although the applied strain at a radius of 3 mm is very high, there are remaining particles in every investigated sample. It is assumed that most of the remaining particles are Co ones.
- The resulting grain sizes of the Cu- and Ag-matrices at a radius of 3 mm are under 100 nm and therefore smaller than in pure HPT deformed Cu and Ag samples.
- The previous annealing treatment does not significantly affect the deformation behaviour and the dissolution of the Co particles in the corresponding matrix, because the microstructure and thus the hardness of the Co phase hardly changed. As a consequence, the annealed samples contain remaining particles as well.
- Nevertheless, a low amount of Fe and Co is dissolved in the matrix at a radius of 3 mm in each investigated sample, and a supersaturated solid solution might be partially created.

Further investigations will address the application of higher amounts of strain. Therefore, the number of revolutions n will be increased from 50 to 100. The higher value of strain might finally lead to a complete dissolution of the Fe and Co particles, although the deformation behaviour is still fragmentation and no co-deformation.

Furthermore, the manufacturing of pre-alloyed powders will be done by a previous MA process. On one hand, it is planned to mill the three powders of one ternary system directly together and deform the consolidated powder sample afterwards by HPT deformation. On the other hand it is planned to mill pure powders of Fe and Co to obtain Fe-Co alloy powders at first and then deform these Fe-Co alloy powders with Cu or Ag powders by HPT.

A further improvement for the production of granular alloys by HPT might be achieved by using different Co powders. For example, one can use a powder from another producer, a powder with a different shape of Co powder particles or a powder with a higher purity. If a powder with an initial higher purity is used, one might obtain a distinct change of the Co microstructure during an annealing treatment.

7. Acknowledgement

First of all, I would like to thank my supervisor Dr. Andrea Bachmaier for giving me the chance to work on this interesting topic. Her support, patience, and wide knowledge in this field were extremely helpful for creating this thesis and enables me a good start for my scientific career.

Furthermore, I would like to thank the Department of Material Physics, especially Prof. Pippan, Dr. Wurster, and DI Stückler, who also support me with their knowledge and experience.

Also, I would like to thank my friends and colleagues for their encouraging words during the period of writing this thesis. It would have been much harder without their mental support. Particularly, I would like to thank Philipp, Julia, and Markus, who are always there for me.

Finally, I would like to thank my family, especially my parents, for supporting my studies at the University of Leoben; they always stand by my side and give me the support I need to achieve my aims in both life and work. Thank you for your parental care throughout my whole life.

8. List of Figures

Figure 1: The Co-Fe phase diagram shows the miscibility of Fe and Co under equilibrium conditions [8].	2
Figure 2: Phase diagrams of the binary systems a) Co-Cu [9], b) Fe-Cu [10], c) Ag-Co [11] and Fe-Ag [12].	3
Figure 3: Schematic representation of a) the HPT equipment [13] and b) the disk shaped sample showing the different observation directions (axial, radial and tangential) [14].	5
Figure 4: BSE micrographs of the microstructure of the deformed $\text{Cu}_{80}(\text{Fe}_{0.5}\text{Co}_{0.5})_{20}$ sample at a radius of a) 0 mm b) 1 mm c) 2 mm and d) 3 mm.	11
Figure 5: Microstructure of the Cu-matrix of the deformed Cu-Fe-Co samples at a radius of 3 mm: a) $\text{Cu}_{80}(\text{Fe}_{0.7}\text{Co}_{0.3})_{20}$ b) $\text{Cu}_{80}(\text{Fe}_{0.5}\text{Co}_{0.5})_{20}$ and c) $\text{Cu}_{80}(\text{Fe}_{0.3}\text{Co}_{0.7})_{20}$.	12
Figure 6: BSE micrographs of the microstructure of the HPT deformed $\text{Ag}_{70}(\text{Fe}_{0.15}\text{Co}_{0.85})_{30}$ sample, taken at a radius of a) 0 mm b) 1 mm c) 2 mm and d) 3 mm.	13
Figure 7: Evolution of the microstructure of the deformed $\text{Ag}_{50}(\text{Fe}_{0.15}\text{Co}_{0.85})_{50}$ sample. BSE micrographs were taken at a radius of a) 0 mm b) 1 mm c) 2 mm and d) 3 mm.	13
Figure 8: Microstructure of the Ag-matrix of the deformed Ag-Fe-Co samples at a radius of 3 mm a) $\text{Ag}_{70}(\text{Fe}_{0.15}\text{Co}_{0.85})_{30}$ b) $\text{Ag}_{70}(\text{Fe}_{0.3}\text{Co}_{0.7})_{30}$ c) $\text{Ag}_{70}(\text{Fe}_{0.5}\text{Co}_{0.5})_{30}$ and d) $\text{Ag}_{50}(\text{Fe}_{0.15}\text{Co}_{0.85})_{50}$.	14
Figure 9: a) Microstructure of the $\text{Cu}_{80}(\text{Fe}_{0.5}\text{Co}_{0.5})_{20}$ sample after annealing for 60 minutes at 500°C. b) Magnified image of a Co particle after the annealing treatment.	15
Figure 10: a) Microstructure of the $\text{Cu}_{80}(\text{Fe}_{0.5}\text{Co}_{0.5})_{20}$ sample after annealing for 30 minutes at 600°C. b) Magnified image of a Co particle after the annealing treatment.	15
Figure 11: a) Microstructure of the $\text{Ag}_{70}(\text{Fe}_{0.15}\text{Co}_{0.85})_{30}$ sample after annealing for 60 minutes at 500°C. b) Microstructure of a Co particle after the annealing treatment.	16
Figure 12: Microstructural evolution of the annealed (500°C, 60 minutes) and HPT deformed $\text{Cu}_{80}(\text{Fe}_{0.5}\text{Co}_{0.5})_{20}$ sample at a radius of a) 0 mm b) 1 mm c) 2 mm and d) 3 mm.	17
Figure 13: Microstructure of the Cu-matrix of the deformed $\text{Cu}_{80}(\text{Fe}_{0.5}\text{Co}_{0.5})_{20}$ samples at a radius of 3 mm a) un-annealed sample b) annealed at 500°C for 60 minutes and c) annealed at 600°C for 30 minutes.	18

Figure 14: Microstructural evolution of the annealed (500°C, 60 minutes) and HPT deformed $\text{Ag}_{70}(\text{Fe}_{0.15}\text{Co}_{0.85})_{30}$ sample at a radius of a) 0 mm b) 1 mm c) 2 mm and d) 3 mm.	18
Figure 15: Microstructure of the Ag-matrix at a radius of 3 mm of the deformed $\text{Ag}_{70}(\text{Fe}_{0.15}\text{Co}_{0.85})_{30}$ sample a) without annealing treatment b) with annealing at 500°C for 60 minutes before HPT deformation.....	19
Figure 16: Images for the phase analysis of the un-annealed and deformed $\text{Cu}_{80}(\text{Fe}_{0.5}\text{Co}_{0.5})_{20}$ sample at a radius of 0 mm a) light optical micrographs b) the corresponding image with the bordered particles.	20
Figure 17: Results of the phase analyses of the deformed $\text{Cu}_{80}(\text{Fe}_{0.5}\text{Co}_{0.5})_{20}$ samples along the radius: a) without previous annealing treatment and b) with annealing at 500°C for 60 minutes.	21
Figure 18: Results of the phase analyses of the deformed $\text{Ag}_{70}(\text{Fe}_{0.15}\text{Co}_{0.85})_{30}$ samples: a) without previous annealing and b) with annealing at 500°C for 30 minutes.....	23
Figure 19: Results of the phase analyses of the deformed $\text{Ag}_{50}(\text{Fe}_{0.15}\text{Co}_{0.85})_{50}$ sample.....	24
Figure 20: Example of an EDX spot measurement: a) SEM micrograph with the marked spot, where the measurement was carried out, b) the measured EDX spectrum and c) the EDX quantification.	25
Figure 21: EDX measurement of a Co particle in the deformed $\text{Cu}_{80}(\text{Fe}_{0.5}\text{Co}_{0.5})_{20}$ sample at a radius of 0 mm: a) SEM micrograph with the marked area where the measurements were performed b) resulting EDX spectrum.....	26
Figure 22: a) SEM micrograph of the annealed and deformed $\text{Cu}_{80}(\text{Fe}_{0.5}\text{Co}_{0.5})_{20}$ sample at a radius of 0 mm and the corresponding EDX maps of b) Cu c) Fe d) Co.	27
Figure 23: a) SEM micrograph of the annealed and deformed $\text{Ag}_{70}(\text{Fe}_{0.15}\text{Co}_{0.85})_{30}$ sample at a radius of 3 mm and the corresponding EDX maps of b) Ag c) Fe d) Co.	28
Figure 24: Microhardness measured along the radius of the HPT deformed samples of the investigated Cu-Fe-Co system: a) Results of the different investigated samples without previous annealing treatment, b) Results of the annealed $\text{Cu}_{80}(\text{Fe}_{0.5}\text{Co}_{0.5})_{20}$ samples compared to the un-annealed sample with the same composition.	29
Figure 25: Microhardness measured along the radius of the HPT deformed samples of the investigated Ag-Fe-Co system: a) Un-annealed samples, b) Comparison of the microhardness of the annealed and un-annealed $\text{Ag}_{70}(\text{Fe}_{0.15}\text{Co}_{0.85})_{30}$ samples.	30

9. List of Tables

Table 1: Overview of the investigated compositions (in at%) of the mixed powders.	8
Table 2: Values of the resulting shear strain γ at different positions in radial direction.....	8
Table 3: Hardness (HV0.05) of the Co particles, the Fe particles and the Cu- and Ag-matrix after various annealing treatments in the $\text{Cu}_{80}(\text{Fe}_{0.5}\text{Co}_{0.5})_{20}$ and $\text{Ag}_{70}(\text{Fe}_{0.15}\text{Co}_{0.85})_{30}$ samples.....	16
Table 4: Quantitative evaluations of the phase analyses of the various samples of the Cu-Fe-Co system.	22
Table 5: Quantitative evaluations of the phase analyses of the various samples of the Ag-Fe-Co system.	23
Table 6: Ideal and actual measured chemical compositions in percent by weight (wt%) of the investigated $\text{Cu}_{80}(\text{Fe}_{0.5}\text{Co}_{0.5})_{20}$ and $\text{Ag}_{70}(\text{Fe}_{0.15}\text{Co}_{0.85})_{30}$ samples.....	25
Table 7: Results of the EDX measurements in wt% of the un-annealed and annealed and deformed $\text{Cu}_{80}(\text{Fe}_{0.5}\text{Co}_{0.5})_{20}$ sample.	27
Table 8: Results of the EDX measurements in wt% of the un-annealed and annealed and deformed $\text{Ag}_{70}(\text{Fe}_{0.15}\text{Co}_{0.85})_{30}$ sample.....	28

10. List of references

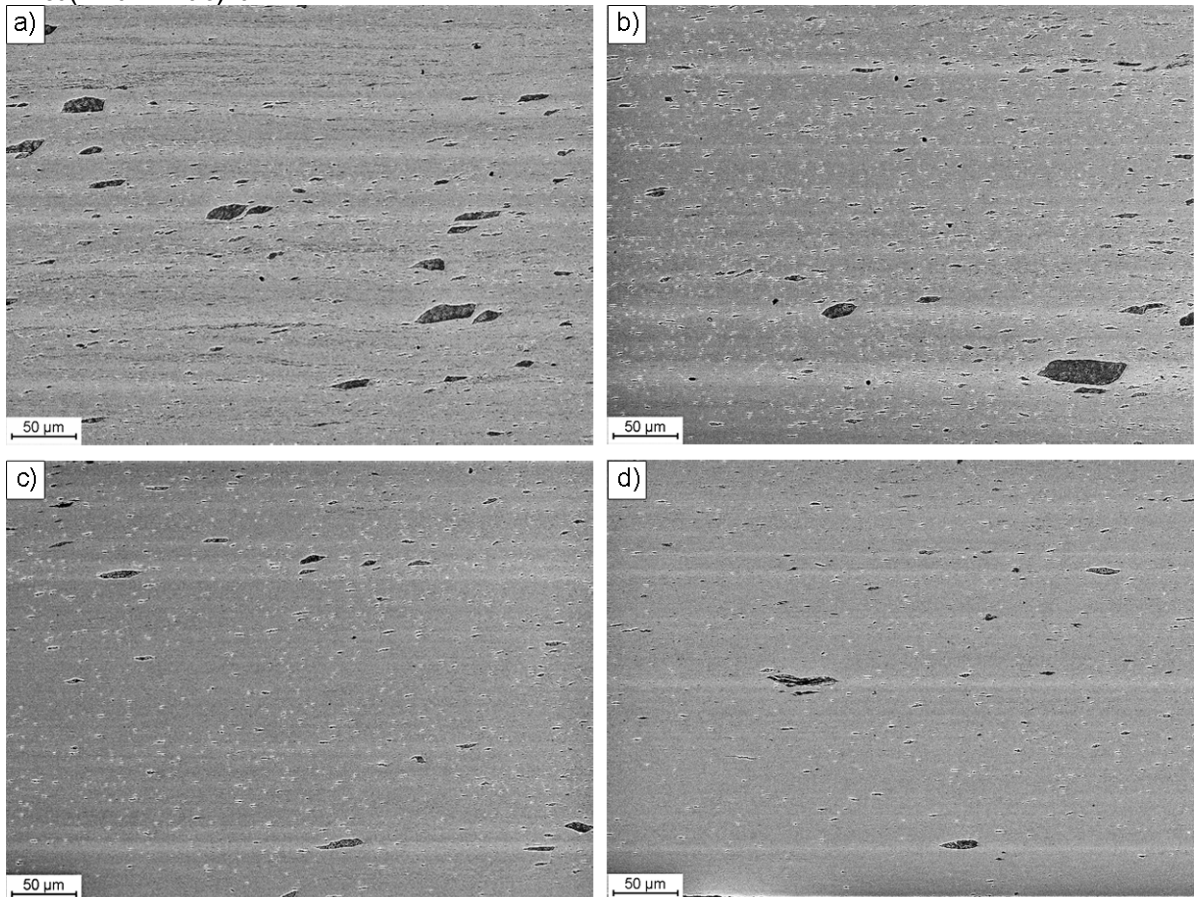
- [1] C. Meneghini, S. Mobilio, A. García-Prieto, M.L.F. Fdez-Gubieda, Structure and magnetic properties in CoCu granular alloys, Nuclear Instruments and Methods in Physics Research Section B: Beam Interactions with Materials and Atoms, Volume 200, 2003, pp. 215-219
- [2] R. Larde´, J.M. Le Breton, Influence of the milling conditions on the magnetoresistive properties of a $\text{Cu}_{80}(\text{Fe}_{0.3}\text{Co}_{0.7})_{20}$ granular alloy elaborated by mechanical alloying, Journal of Magnetism and Magnetic Materials, 2005, pp. 1120-1122
- [3] L. Chang, M. Wang, L. Liu, S. Luo, P. Xiao, A brief introduction to giant magnetoresistance, arXiv:1412.7691, 2014, pp. 1-11
- [4] N. S. Cohen, Q. A. Pankhurst and L. F. Barquín, Structural and magnetoresistive properties of mechanically alloyed Fe–Co–Ag, Journal of Physics., Condensed Matter 11, 1999, pp. 8839-8853
- [5] K. S. Kormout, R. Pippan and A. Bachmaier, Deformation-Induced Supersaturation in Immiscible Material Systems during High-Pressure Torsion, Advanced Engineering Materials , 2016, pp. 1-19
- [6] C. Suryanarayana, Mechanical alloying and milling, Progress in Materials Science 46, 2001, pp. 1-184
- [7] S. Ikeda, T. Houga, W. Takakura, Y. Ueda, Magnetoresistance in $(\text{Co}_x\text{Fe}_{1-x})_{20}\text{Cu}_{80}$ granular alloys produced by mechanical alloying, Materials Science and Engineering A217/218, 1996, pp. 376-380
- [8] <http://www.himikatus.ru/art/phase-diagr1/Co-Fe.php> (04.06.2018)
- [9] <http://www.himikatus.ru/art/phase-diagr1/Co-Cu.php> (04.06.2018)
- [10] <http://www.himikatus.ru/art/phase-diagr1/Cu-Fe.php> (04.06.2018)
- [11] <http://www.himikatus.ru/art/phase-diagr1/Ag-Co.php> (04.06.2018)
- [12] <http://www.himikatus.ru/art/phase-diagr1/Ag-Fe.php> (04.06.2018)
- [13] R. Pippan, S. Scheriau, A. Taylor, M. Hafok, A. Hohenwarter, A. Bachmaier, Saturation of Fragmentation During Severe Plastic Deformation, Annual Review of Materials Research, 2010, pp. 319-343
- [14] R. Pippan, F. Wetscher, M. Hafok, A. Vorhauer, I. Sabirov, The Limits of Refinement by Severe Plastic Deformation, Advanced Engineering Materials, 2006, pp. 1046-1056
- [15] H.P. Stüwe, Equivalent Strains in Severe Plastic Deformation, Advanced Engineering Materials, 2003, pp. 291-295

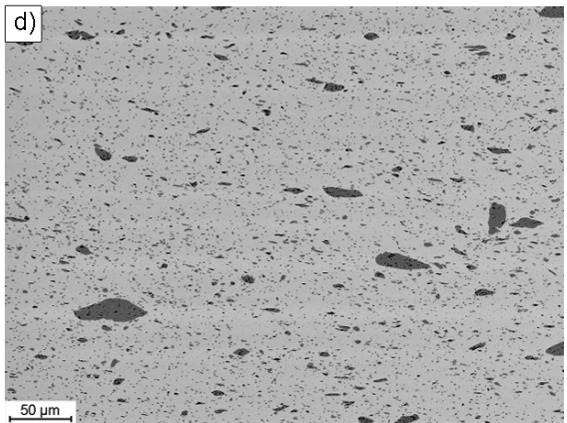
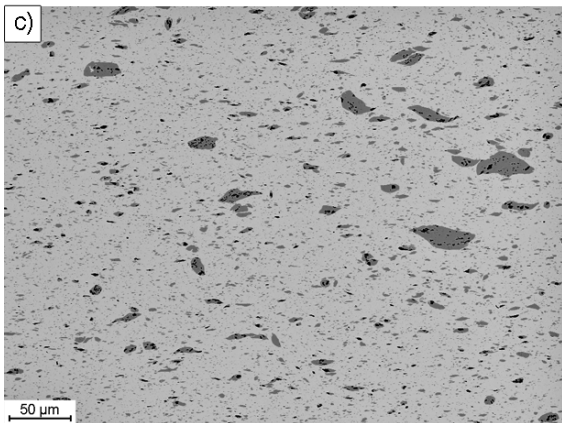
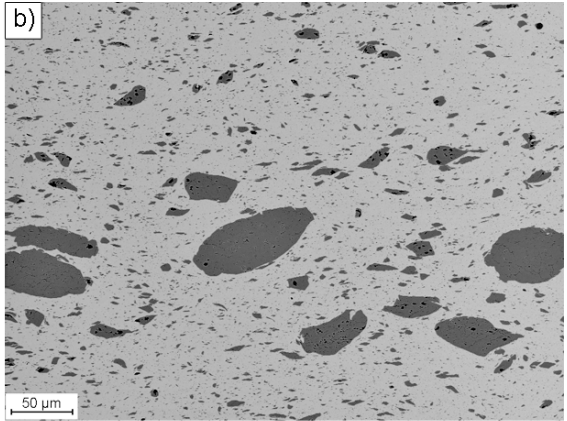
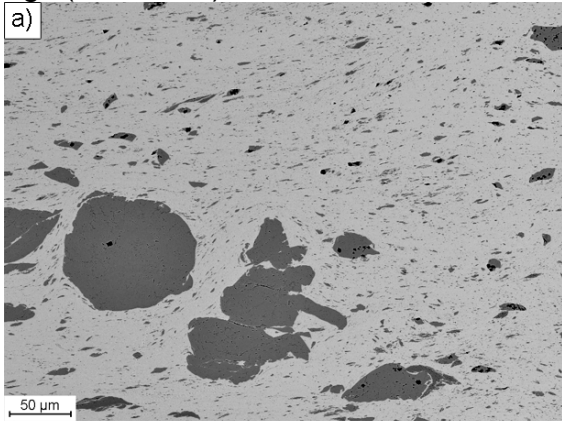
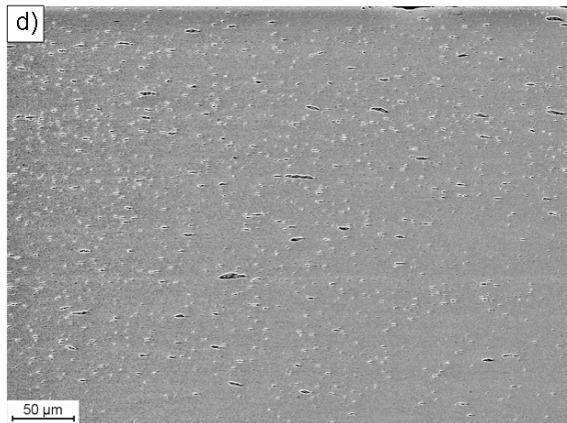
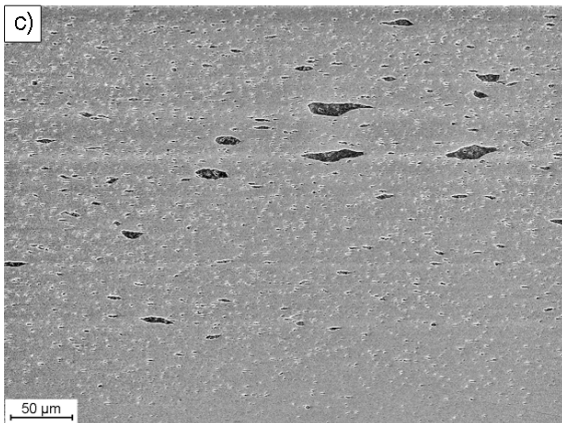
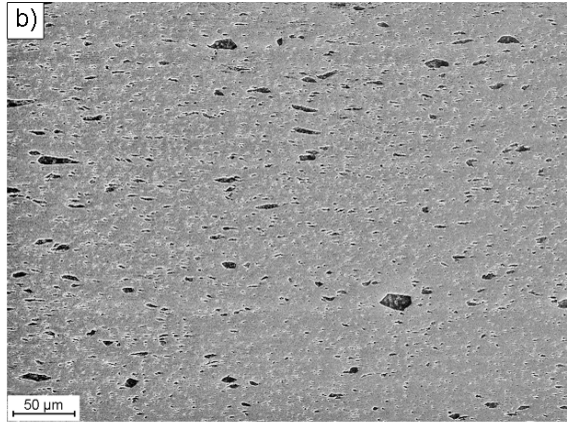
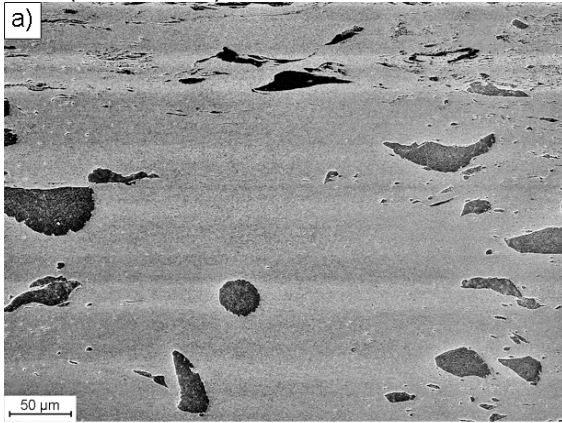
- [16] A. Hohenwarter, A. Bachmaier, B. Gludovatz, S. Scheriau, R. Pippan, Technical parameters affecting grain refinement by high pressure torsion, *International Journal of Materials Research*, 2009, pp. 1653-1661
- [17] A. Bachmaier, R. Pippan, Generation of metallic nanocomposites by severe plastic deformation, *International Materials Reviews*, 2013, vol 58, no 1, pp. 41-62
- [18] W. Pabst, E. Gregorová, Characterization of particles and particle systems, ITC Prague, 2007, p. 27
- [19] K. S. Kormout, B. Yang, R. Pippan, Deformation Behavior and Microstructural Evolution of Cu-Ag Alloys Processed by High-Pressure Torsion, *Advanced Engineering Materials*, 2015, pp. 1828-1834

11. Appendix

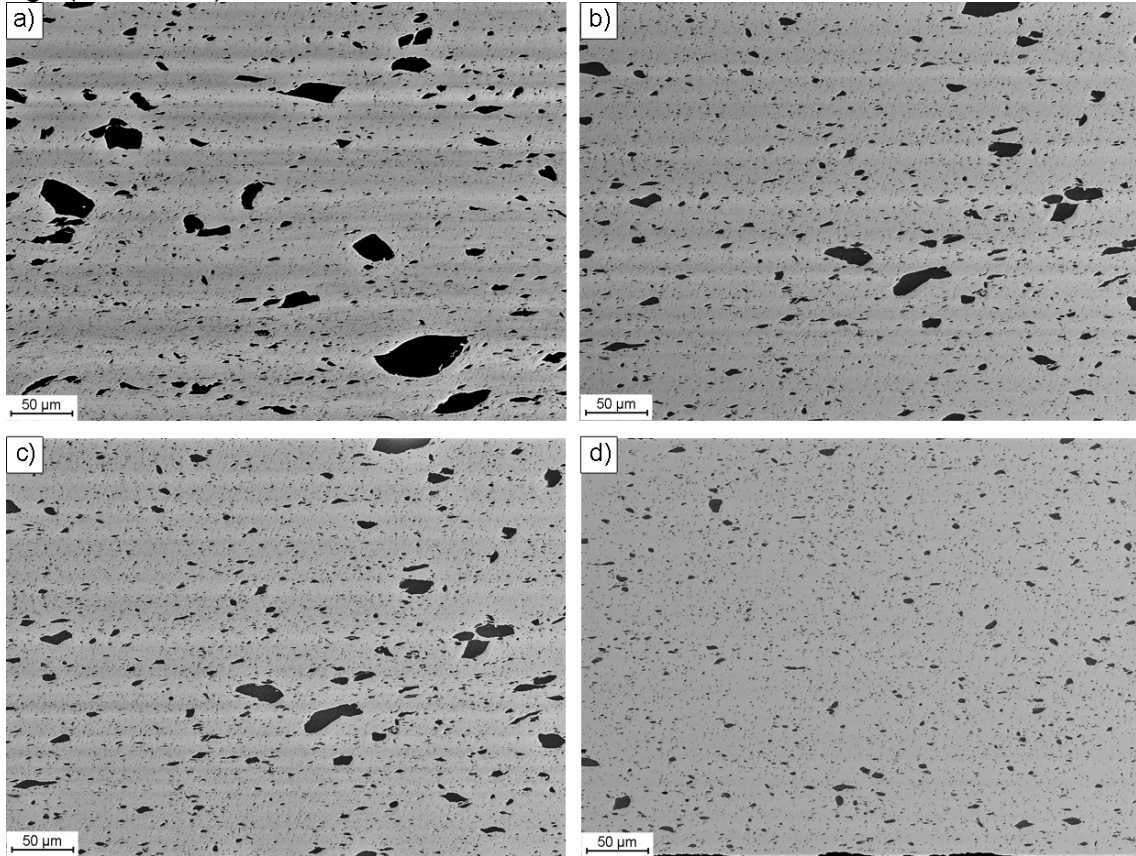
11.1. Evolution of the microstructure

In the following, the evolution of the microstructure of further samples of the ternary systems Cu-Fe-Co and Ag-Fe-Co are shown. The BSE micrographs of all samples were taken at a radius of 0 mm (a), 1 mm (b), 2 mm (c), and 3 mm (d).

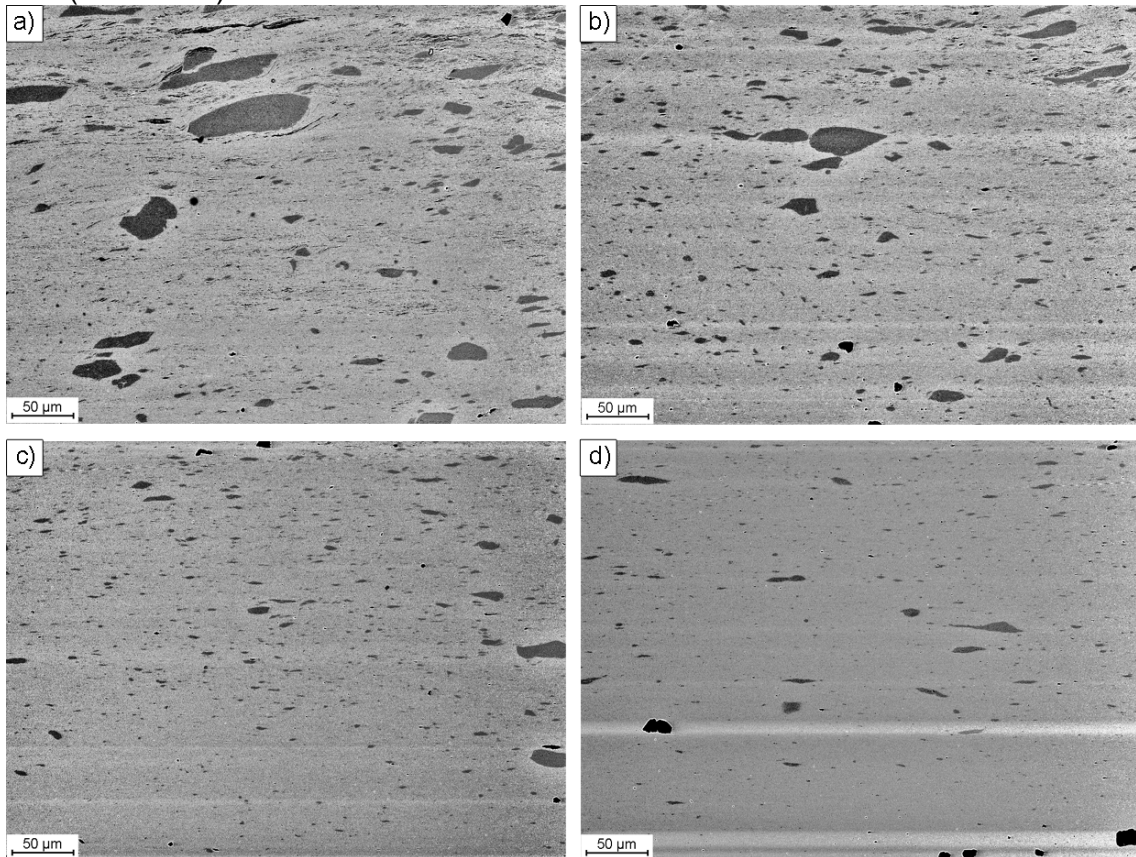




$\text{Ag}_{70}(\text{Fe}_{0.5}\text{Co}_{0.5})_{30}$



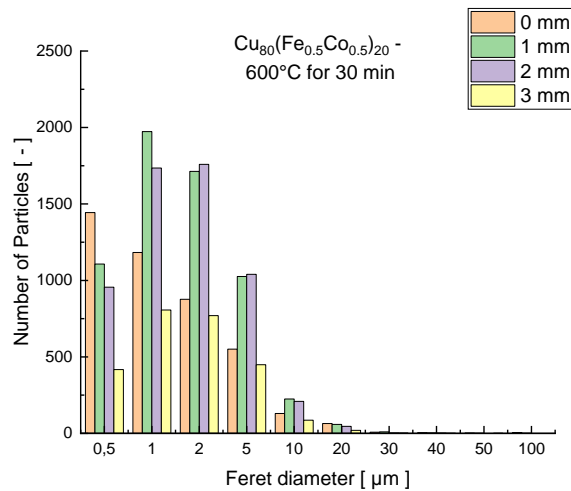
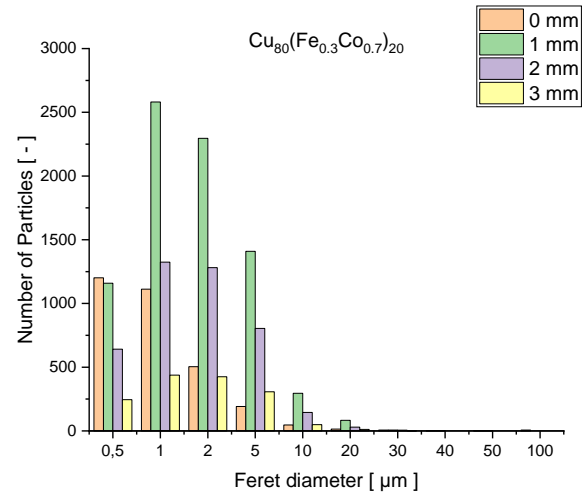
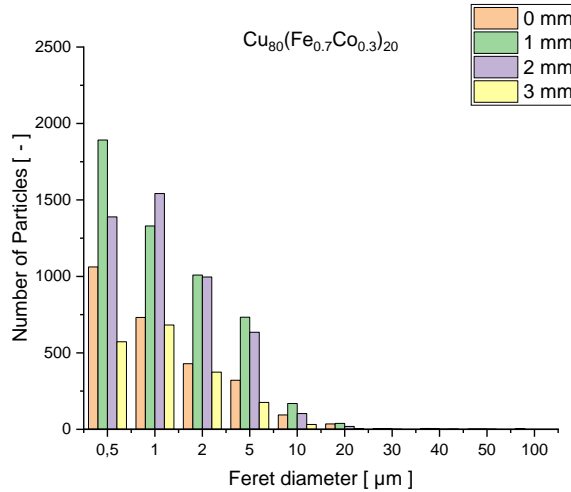
$\text{Cu}_{80}(\text{Fe}_{0.5}\text{Co}_{0.5})_{20}$ – 600°C for 30 minutes



11.2. Results of the phase analysis with ImageJ

In the following, the results of the phase analyses with ImageJ of further investigated samples are shown. The histograms display the number of detected particles for different ranges of feret diameter at different radii.

Cu-Fe-Co system



Ag-Fe-Co system

